

Advanced composite materials

R. PYRZ

*Aalborg University
Institute of Mechanical Engineering
Pontoppidanstraede 101, DK-9220 Aalborg, Denmark*

These notes provide a brief introduction to different modelling approaches used to describe coupled multi-physics processes in solids. Examples of typical processing-related application areas, and the disciplines required to develop appropriate predictive models are given. This is then followed by an example of a coupled multi-physics constitutive framework recently developed to study the failure of ceramic-metal interfaces undergoing oxidation and subjected to thermal fatigue. In this example, system failure occurs by cleavage due to the nucleation and coalescence of mesoscopic cracks within the ceramic-metal bimaterial system. Such bimaterial systems are usually present in thermal barriers coatings used in gas turbine blade applications. The magnitudes of the peak local stresses normal to the bimaterial interface, which are responsible for microcrack nucleation during thermal cycling, are determined from a multi-scale continuum mechanics parametric study. The finite element studies rely on the coupled diffusion-constitutive framework and periodic unit cell techniques to incorporate explicitly the effects of interface morphology, oxidation and time-dependent deformation processes on the local interfacial stresses.

1. Introduction

Composite materials are hybrid materials of which the composition and internal architecture are varied in a controlled manner in order to match their performance to the most demanding structural or non-structural roles. The composite microstructures may be subdivided, as depicted in Fig. 1, according to whether the reinforcement is in the form of continuous fibres, short fibres, or particles. Further distinction may be drawn on the basis of fibre diameter, orientation distribution and the matrix and inclusions constituent materials i.e. metal, polymer, ceramic.

Most materials are effective composites. This is particularly true of natural biological materials, which are often made up of at least two constituents. In many cases, a strong and stiff *component* is present, often in elongated form, embedded in a softer constituent forming the matrix. For example, wood is made up of fibrous chains of cellulose molecules in a matrix of lignin, while bone and teeth are both essentially composed of hard inorganic crystals (hydroxyapatite) in a matrix of a tough organic constituent called collagen.

An interesting example is provided by the so-called “dual phase” steels evolved in the seventies. They are produced by annealing fairly low carbon steels in the $\alpha + \gamma$ phase field and then quenching so as to convert the γ phase to martensite. The result is a product very close to what is now referred to as a particulate composite with

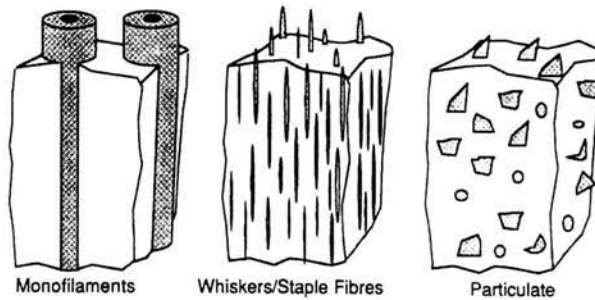


FIGURE 1. Schematic depiction of the three types of composites, classified according to the type of reinforcement.

about 20% of very hard, relatively coarse martensite particles distributed in a soft ferrite matrix. This is a strong, tough and formable material, now used extensively in important applications such as car bodywork. Its success could be interpreted as confirming the viability of the composite concept, although its properties have been very seldom considered in terms of composite micromechanics.

A composite might seem a case of needless complexity. The making of ideal structural materials would appear to be at hand, in the midsection of the periodic table. Those elements, among them carbon, aluminium, silicon, nitrogen and oxygen form compounds in which atoms are joined by strong and stable bonds. As a result, such compounds typified by the ceramics, for instance aluminium oxide, silicon carbide and silicon dioxide, are strong, stiff and resistant to heat and chemical attack. Their density is low and furthermore their constituent elements are abundant.

Yet because of a serious handicap these substances have rarely served as structural materials. They are brittle and susceptible to cracks. In bulk form the substance is unlikely to be free of small flaws or to remain free of them for long in actual use. When such a material is produced in the form of fine fibres, its useful strength is greatly increased. The remarkable increase in strength at small scales is in part a statistical phenomenon. If one fibre in an assemblage does fail, moreover, the crack cannot propagate further, and the other fibres remain intact. In a similar amount of the bulk material, in contrast, the initial crack might have led to complete fracture.

Tiny needlelike structures called whiskers made of substances such as silicon carbide and aluminium oxide also contain fewer flaws and show greater strength than the material in bulk form. Whiskers are less likely to contain defects than the bulk material, not only for statistical reasons, but also because they are produced as single crystals having a theoretically perfect geometry. The notion that many materials perform best as fibres also holds for certain organic polymers. Composites are a strategy for producing advanced materials taking advantage of the enhanced properties of inclusions. A bundle of fibres has little structural value. To harness their strength in a practical material the designer of a composite embeds them in a matrix of another material. The matrix acts as an adhesive, binding the fibres and lending solidity to the material. It also protects the fibres from environmental stress and physical damage which could initiate cracks.

The strength and stiffness of the composite remain very much a function of the reinforcing material, but the matrix makes its own contribution to properties. The ability of the composite material to conduct heat and current, for example, is heavily influenced by the conductivity of the matrix. The mechanical behaviour of the composite is also governed, not by the fibres alone, but by a synergy between the fibres and the matrix.

The ultimate tensile strength of a composite is a product of the synergy. When a bundle of fibres without a surrounding matrix is stressed, the failure of a single fibre eliminates it as a load carrier. The stress it had borne shifts to the remaining intact fibres moving them closer to failure. If the fibres are embedded in a matrix, on the other hand, fracture does not end the mechanical function of a fibre. The reason is that as the broken ends of the fibre pull apart, elastic deformation or plastic flow of the matrix exerts shear forces gradually building stress back into the fragments. Because of such load transfer the fibre continues to contribute some reinforcement to the composite. The stress on the surrounding intact fibres increases less than it would in the absence of the matrix, and the composite is able to bear more stress without fracturing. The synergy of the fibres and the matrix can thus strengthen the composite and also toughen it by increasing the amount of work needed to fracture it.

Although the general requirement that the matrix will be ductile provides some guidance for choosing a matrix material, the most common determinant of the choice is the range of temperatures the composite will face in its intended use. Composites exposed to temperatures between 100 and 200°C usually have a matrix of polymer. Most composites belong to this group.

Polymer matrices are often thermosets. They are polymers in which bonds between the polymer chains lock the molecular structure in a rigid three-dimensional network, which cannot be melted. Thermosets resist heat better than most thermoplastics, the other class of polymeric materials, which melt when they are heated because no bonds cross-link the polymer chains. Epoxies are the most common thermosetting matrix for high-performance composites, but a class of resins called polyimides, which can survive continuous exposure to temperatures of more than 300°C, have attracted considerable interest. If the resin is a thermoset, the structure must then be cured, subjected to conditions that enable the polymer chain to cross-link. Often the composite must be held at high temperature and pressure for many hours.

In part to shorten the processing time, thermoplastic matrix materials are attracting growing interest; one promising example is a polymer called PEEK (polyetheretherketone). Consolidating a composite that has a thermoplastic matrix requires only relatively short exposure to a temperature which is sufficient to soften the plastic. The melting temperature of some thermoplastic matrices is so high that they rival thermosets in heat resistance; PEEK, for example, melts at 334°C. Thermoplastics have the additional advantage of being tougher than most of the thermosets.

Temperatures high enough to melt or degrade a polymer matrix call for another kind of matrix material, often metal. Along with temperature resistance a metal matrix offers other benefits. Its higher strength supplements that of the reinforcing fibres, and its ductility lends toughness to the composite. A metal matrix exacts

two prices: density that is high in comparison with polymers, even though the light metals such as aluminium, magnesium and titanium are the most common matrices, and complexity of processing. Indeed, whereas the production of many advanced polymer matrix composites has become routine, the development of metal matrix composites has progressed more slowly in part because of the extreme processing conditions needed to surround high strength fibres with a matrix of metal.

Metal matrix composites might assume a place in the cooler parts of the skin of a hypersonic aircraft, but at the nose, on leading edges of the wings and in the engines, temperatures could exceed the melting point of a metal matrix. For these environments there is a growing interest in a class of composites that have matrices as resistant to heat as the fibres themselves, and also as lightweight and potentially as strong and stiff, namely, ceramics. Because they are brittle, ceramics behave differently from other matrices. In metal and polymer matrix composites the fibres supply most of the strength, and the ductile matrix acts to toughen the system. A ceramic matrix, in contrast, is already abundantly stiff and strong, but to realize its full potential it needs toughening. The fibres in a ceramic matrix composite fill this need by blocking the growth of cracks. A growing crack which encounters a fibre may be deflected or may pull the fibre from the matrix. Both processes absorb energy.

The ceramic matrix gives such composites great temperature resistance. Borosilicate glass reinforced with carbon fibres retains its strength at 600°C. Such matrices as silicon carbide, silicon nitride, aluminium oxide or mullite (a complex compound of aluminium, silicon and oxygen) yield composites that remain serviceable at temperatures well above 1000°C. The heat resistance of a ceramic matrix composite, however, complicates its fabrication.

The characteristics of these three classes of composites can be exemplified by the relation of stress and strain for the unreinforced polymer, metal and ceramic as compared with curves for the corresponding composites. Whereas unreinforced epoxy stretches easily, an epoxy matrix composite containing 50% by volume of silicon carbide fibres is far stiffer (Fig. 2a). In an aluminium matrix the same volume of reinforcement, in this case aluminium oxide fibres, also improves stiffness dramatically (Fig. 2b). Because the fibres are brittle the composite fails at a much lower strain than unreinforced aluminium does. A similar fraction of silicon carbide fibres stiffens a matrix of borosilicate glass only slightly but toughens it considerably, increasing the percentage by which it can be strained without breaking (Fig. 2c). The fibres do so by restraining the growth of matrix cracks which might otherwise lead to fracture.

Related to ceramic matrix composites in character but distinctive in manufacture is a composite in which both the matrix and the reinforcing fibres consist of elemental carbon. Carbon-carbon composite is reinforced by the element in a semicrystalline form, graphite; in the matrix the carbon is mostly amorphous. A carbon-carbon composite retains much of its strength at 2500°C and is used in the nose cones and heat shields of re-entry vehicles. Unlike most ceramic composites, it is vulnerable to oxidation at high temperatures. A thin layer of ceramic is often applied to the surface of a carbon-carbon composite to protect it.

The combination of fibre and matrix gives rise to an additional constituent in composites; an interphase region. Chemical compatibility between the fibres and

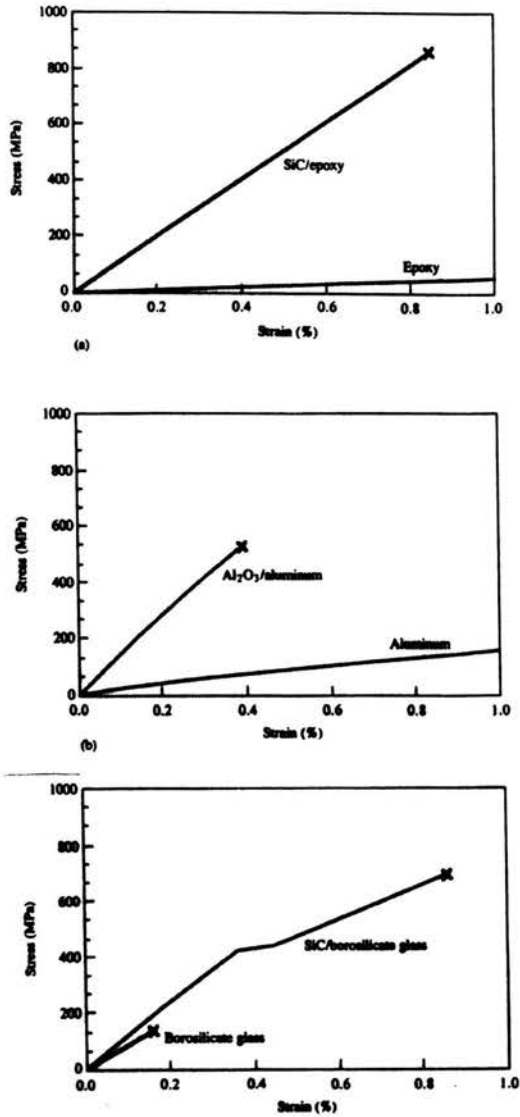


FIGURE 2. Stress-strain curves for (a) SiC/epoxy, (b) Al₂O₃/aluminium, and (c) SiC/borosilicate glass composites.

the matrix is most crucial at this region. In polymer and metal matrix composites a bond must develop between the reinforcement and the matrix, if they are to act in concert. A prerequisite for adhesion is that the matrix, in its fluid form, will be capable of wetting the fibres. Fibres that would otherwise not be wetted by their matrix can be given a coating that fosters contact by interacting with both the fibres and the matrix. In some cases varying the matrix composition can also promote the

process. Once the matrix has wetted the fibres thoroughly, intermolecular forces or chemical reactions can establish the bond.

Progress towards managing the many variables of composite design has encouraged investigators to contemplate new complexities. An ordinary composite reinforced with stiff, straight fibres usually displays a nearly constant value of stiffness. New composites designed to display specific non-linear relations of strain and stress are now attracting interest. One such example, a flexible composite consisting of undulating fibres in an elastomeric matrix, can elongate readily at low stresses, but stiffens when the fibres become fully extended, Fig. 3.

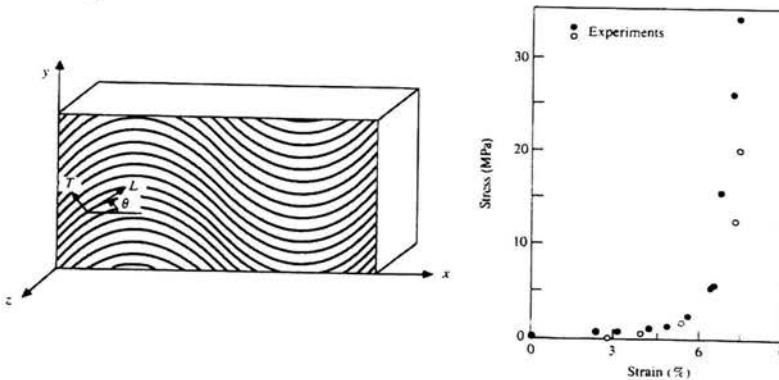


FIGURE 3. Flexible unidirectional composite and corresponding stress-strain diagram along x axis.

A hybrid composite strengthened with two kinds of fibres, some of them brittle and inextensible and the other ductile and tough, can display the opposite behaviour. The stiff fibres cause stress to increase very sharply at low strains, but when the strain is sufficient to break the stiff, brittle fibres, the curve of stress over strain flattens, Fig. 4. The ductile fibres come into play, and as a result the composite becomes more extensible. The hybrid design can yield a material that combines much of the stiffness of an ordinary composite containing only stiff fibres with increased toughness.

Traditionally, composites have been designed and manufactured with the purpose of serving very specific functional goals. Such goals and considerations may include stiffness, fracture, toughness, fatigue life, impact resistance, electromagnetic shielding, corrosion resistance and biocompatibility, just naming a few. With the expansion in available material systems for composites, advancements in fabrication technologies and improvements in analysis and design techniques, it becomes increasingly feasible for developing *multi-functional* fibre composites for which a number of functional goals are satisfied simultaneously, and the performance can be optimized. It should be born in mind that multifunctional composites are made possible only through the *design of their microstructure*. For example the transport properties e.g. electrical conductivity, thermal conductivity, dielectric constants, magnetic permeability and diffusion coefficients of composites are also very sensi-

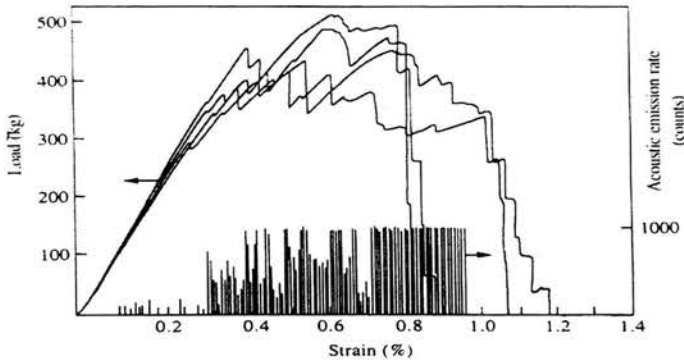


FIGURE 4. Tensile stress-strain curves of a carbon/glass/epoxy interlaminated composite.

tive to the microstructure. Consider, for instance, the electrical behaviour of metal-filled polymers. The effective resistivity changes sharply from non-conducting to conducting behaviour upon crossing a "percolation threshold" demonstrating the importance of structural features that promote transport along the preferred path, i.e. percolative mechanisms. Figure 5 illustrates such a transition for a composite containing conductive fillers in an insulating polymer matrix. The decrease in resistivity with the increase in filler volume fraction is attributed to the enhancement in probability of particle-particle contact. These contacts promote the formation of continuous conduction paths that mimic the behaviour of conducting fibres.

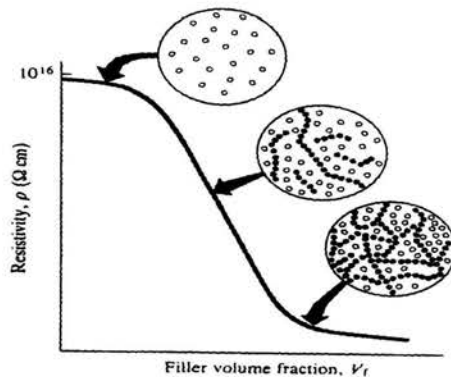


FIGURE 5. Chain formation in a particulate filled composite. Open circles and closed circles indicate, respectively, isolated particles and contacting particles participating in chain formation.

It is important to recognize that the distinction between the three classes of materials i.e. metals, ceramics and polymers and their composites is disappearing. There are now plastics as strong as metals which show some electrical conductivity. Metal is being made as super-plastic and can be subjected to deformation in

processing like conventional polymeric materials. Also the three classes of materials are beginning to show the same limits of strength and stiffness; fibres made from all three can attain stiffness and strength close to the theoretically predicted values. Furthermore, the properties of all three classes of materials can be modified and improved by the use of surface coatings.

As the distinction between the three classes of materials disappears, new possibilities and opportunities arise. One of these is the possibility of designing materials

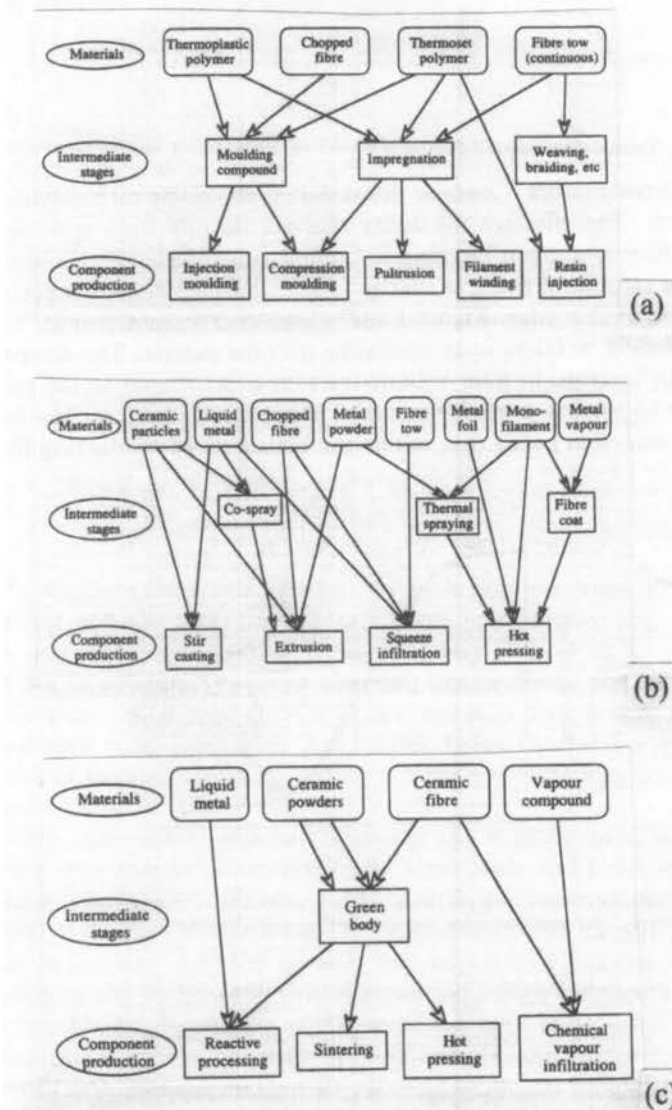


FIGURE 6. Schematic overview of the approaches employed in fabrication of (a) polymer matrix composites, (b) metal matrix composites, and (c) ceramic matrix composites.

not so much for final properties but equally in terms of processability. Figure 6 illustrates approaches used in processing of composites for three classes of materials.

The commonality in some processing routes shared by the three classes of materials will enable more extensive and effective transfer of know-how among the three basic disciplines and effect efficient processing technology for composite materials. Furthermore, the commonality in performance shared by the three classes of materials, e.g. stiffness, strength and thermal expansion enables to engineer composites with a broad spectrum of component materials. Consequently, hybridization of materials, e.g. glass and low-melting-point metal, ceramics and thermoplastics, and polymer and metal in laminates, or other interdispersed composite forms can be achieved and the properties optimized (e.g. composites composed of metal and

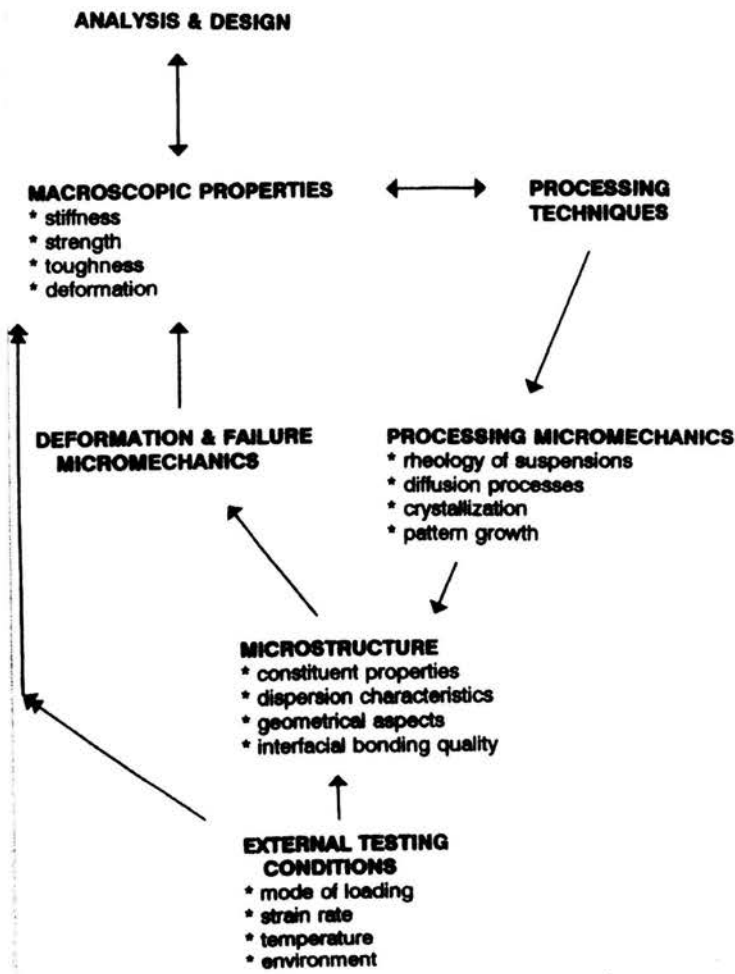


FIGURE 7. Integrated design methodology.

polymer components of nearly the same stiffness but different fatigue resistance or thermal expansion coefficient).

The traditional approach based upon discrete design and manufacturing steps for conventional structural materials needs to be replaced by an integrated design and manufacturing process, which necessitates a closer relationships among different disciplines of materials technology, Fig. 7.

A fully integrated design process capable of balancing all the relevant design, material and manufacturing variables requires an extensive data base on *microstructure constitution and behaviour*, the ability to model fabrication processes, and three-dimensional analysis of the properties and behaviour of the resulting structure. Knowledge of the *relationships among the constituent properties, microstructure and macroscopic behaviour* of the composite is basic to the development of an integrated design methodology. The similarity in material property and behaviour of the three classes of materials implies that *analytical and design methodologies* originally developed for a specific class of composites *may be transferable* to others. A notable example is the fracture and failure behaviour of ceramic and polymer based composites.

These notes are intended as a short introduction to micromechanics of heterogeneous materials, modelling and characterization techniques which encompass all three classes of materials and their composites.

2. Effective properties – simple models

Composite materials are inherently inhomogeneous in terms of both elastic and inelastic properties. One consequence of this is that, on applying a load, a non-uniform distribution of stress is set up within the composite. Much effort has been devoted to understanding and predicting this distribution, as it determines how the material will behave and can be used to explain the superior properties of composites over conventional materials. The methods used for modelling stress distribution in composites range widely in nature and complexity.

2.1. The slab model

The simplest way to model the behaviour of a composite containing continuous aligned fibres is to treat it as if it were composed of two slabs bonded together, one of the matrix and the other of the reinforcement, with the relative thickness of the latter in proportion to the volume fraction of the fibres (designated as f). The response of this "composite slab" to external loads can be predicted quite easily, but its behaviour will closely mirror that of the real composite only under certain conditions.

2.1.1. Axial stiffness. The model is most useful for the case of a normal stress being applied parallel to the fibre axis (the 1-direction), Fig. 8. The two slabs are constrained to have the same lengths parallel to the bonded interface. On applying a stress σ_1 the two components of the slab composite exhibit the same strain ϵ_1 . This "equal strain" condition is valid for loading along the fibre axis, provided that there is no interfacial sliding. The axial strain in the fibre and the matrix must

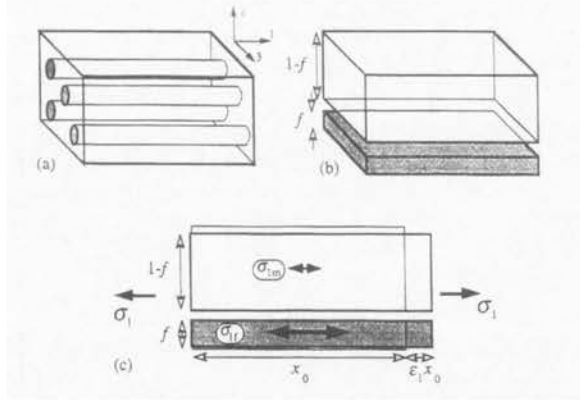


FIGURE 8. Schematic illustration of (a) a composite with aligned fibres, (b) a representation of this as bonded slabs containing a volume fraction f of fibres, and (c) the two slabs experience the same axial strain.

correspond to the ratio between the stress and the Young’s modulus for each of the two components so that

$$\epsilon_1 = \epsilon_{1f} = \frac{\sigma_{1f}}{E_f} = \epsilon_{1m} = \frac{\sigma_{1m}}{E_m}. \tag{2.1}$$

Hence, for a composite in which the fibres are much stiffer than the matrix ($E_f \gg E_m$), the reinforcement is subject to much higher stresses ($\sigma_{1f} \gg \sigma_{1m}$) than the matrix and there is a redistribution of the load. The overall stress σ_1 can be expressed in terms of the two contributions being made

$$\sigma_1 = (1 - f) \sigma_{1m} + f \sigma_{1f}. \tag{2.2}$$

The Young’s modulus of the composite can now be written

$$E_1 = \frac{\sigma_1}{\epsilon_1} = \frac{[(1 - f) \sigma_{1m} + f \sigma_{1f}]}{\sigma_{1f}/E_f} = E_f \left[\frac{(1 - f) \sigma_{1m}}{\sigma_{1f}} + f \right].$$

Using the ratio between the stresses in the components given by Eq. (2.1), this simplifies to Using the ratio between the stresses in the components given by Eq. (2.1), this simplifies to

$$E_1 = (1 - f) E_m + f E_f. \tag{2.3}$$

This well known “Rule of Mixtures” indicates that the composite stiffness is simply a weighted mean between the moduli of the two components, depending only on the volume fraction of fibres. This equation is expected to be valid to a high degree of precision, providing the fibres are long enough for the equal strain assumption to apply. Very minor deviations from the equation are expected as a result of stresses which arise when the Poisson’s ratios of the two components are not equal. The equal strain treatment is often described as a “Voigt model”.

2.1.2. Transverse stiffness. Prediction of the transverse stiffness of a composite from the elastic properties of the constituents is far more difficult than the axial value. In addition, experimental measurement of transverse stiffness is more prone to error, as a result of higher stresses in the matrix, which can, for example, cause polymeric matrices to creep under modest applied loads. The conventional approach is to assume that the system can again be represented by the slab model depicted in Fig. 9.

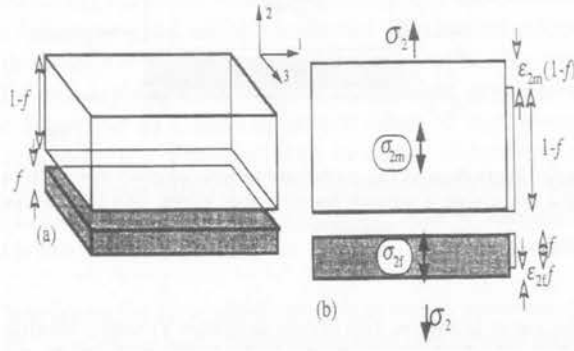


FIGURE 9. Schematic showing (a) the slab model and (b) the "equal stress" assumption.

An obvious problem with the slab model is that the 2- and 3-directions are not identical; direction 3 is equivalent to the axial direction. In reality, the matrix is subjected to an effective stress intermediate between the full applied stress operation on the matrix when it is normal to the plane of the slab interface and the reduced value calculated above for a stress axis parallel to this interface. In the limiting case of the "equal stress" model a stress is applied in the 2-direction

$$\sigma_2 = \sigma_{2f} = \varepsilon_{2f} E_f = \sigma_{2m} = \varepsilon_{2m} E_m, \quad (2.4)$$

so that the component strains can be expressed in terms of the applied stress. The overall net strain can be written as

$$\varepsilon_2 = f\varepsilon_{2f} + (1-f)\varepsilon_{2m} \quad (2.5)$$

from which the composite modulus is given by

$$E_2 = \frac{\sigma_2}{\varepsilon_2} = \frac{\sigma_{2f}}{[f\varepsilon_{2f} + (1-f)\varepsilon_{2m}]}.$$

Substituting expressions for ε_{2f} and ε_{2m} derived from (2.4) gives

$$E_2 = \left[\frac{f}{E_f} + \frac{(1-f)}{E_m} \right]^{-1}. \quad (2.6)$$

The equal stress treatment is often described as a "Reuss model".

Although this treatment is simple and convenient it gives a poor approximation for E_2 . It is instructive to consider the true nature of stress and strain distributions during this type of loading when the "slab" of reinforcement is replaced by fibres. In simple terms, regions of the matrix "in series" with the fibres, close to them and in line along the loading direction, are subjected to a high stress similar to the one carried out by reinforcement as depicted in Fig. 9b. The regions of the matrix "in parallel" with the fibres, i.e. adjacent laterally, are constrained to have the same (low) strain as the reinforcement and carry a low stress as illustrated by Fig. 8c.

The overall strain field can be visualized by the operations of removing the fibres, uniformly straining the remaining matrix, re-insert the fibres (which will be very little deformed by the stress, as they have a high stiffness), and then distorting the matrix so as to re-unite the two components around the interfaces. The result of this operation is shown in Fig. 10; the grid lines, which initially form a square mesh to represent unstrained material, become distorted on loading the composite in a way which reveals the distribution of local strain. This strain, and hence the stress, is distributed inhomogeneously within the matrix - in contrast to the uniformity of matrix strain when the loading direction is along the fibres. This inhomogeneity, with sharp concentrations of stress in certain locations, is very significant in terms of the onset of non-elastic behaviour, which arises as a result of interfacial debonding, matrix plastic deformation and microcracking. The general nature of the transverse strain field is provided by the photoelastic technique applied to a macromodel composite material loaded normal to the fibre direction (vertically in the image shown in Fig. 11).

The higher order fringes, which are located above and below the fibres, represent regions in which the matrix is highly distorted. The sharp gradients of stress along the loading direction form an important feature: most simple attempts to represent the distribution of matrix stress, such as the slab model, do not take this into account.

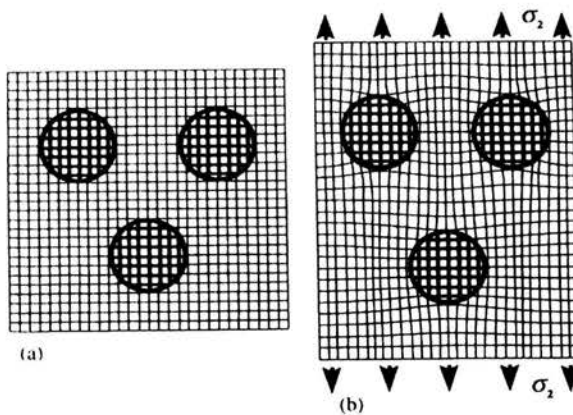


FIGURE 10. Schematic strain field (a) unstrained and (b) on application of a transverse stress in the vertical direction.

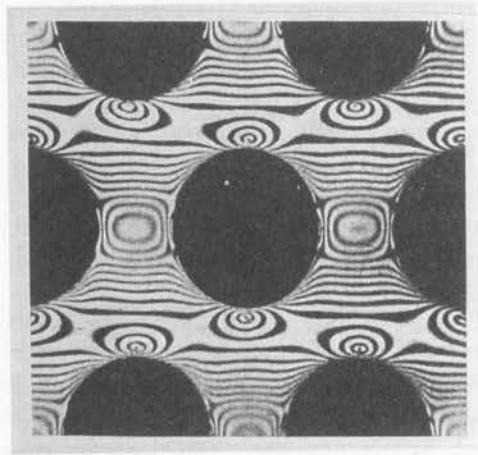


FIGURE 11. A photoelastic image showing isochromatic fringes for a macro-model composite loaded in transverse tension (vertical direction).

The slab model gives an underestimate of the Young's modulus and can be treated as a lower bound. Various empirical and semi-empirical expressions designed to give more accurate estimates have been proposed. The most successful of these is following (the Halpin-Tsai equation)

$$E_2 = \frac{E_m(1 + \xi \eta f)}{(1 - \eta f)}, \quad (2.7)$$

in which

$$\eta = \frac{\left(\frac{E_f}{E_m} - 1\right)}{\left(\frac{E_f}{E_m} + \xi\right)}.$$

The value of ξ may be taken as an adjustable parameter, but its magnitude is generally of the order of unity.

A comparison is presented in Fig. 12 between the predictions of Eqs. (2.3), (2.6) and (2.7) and experimental data for a glass/polyester system. It is clear that the equal strain treatment (Eq. (2.3)) is in close agreement with data for the axial modulus. For the transverse modulus, the situation is less clear.

Firstly, the experimental data show considerable scatter; some of the values actually lie below the equal stress prediction, Eq. (2.6), which should constitute a lower bound. Secondly, many of the values appear to lie closer to the equal stress curve than to the Halpin-Tsai prediction, although this is less obvious for the high fibre content. This behaviour is almost certainly the result of inelastic deformation of the matrix. In practice, the behaviour may be influenced by other factors which are difficult to incorporate into simple models. These include the effect of a degree of fibre misalignment, elastic anisotropy of the fibre (or of the matrix - e.g. for a textured polycrystalline metal) or the early onset of a non-elastic response. Nevertheless, it should be noted that even in the absence of any such complications, use of the equal stress model introduces significant errors.

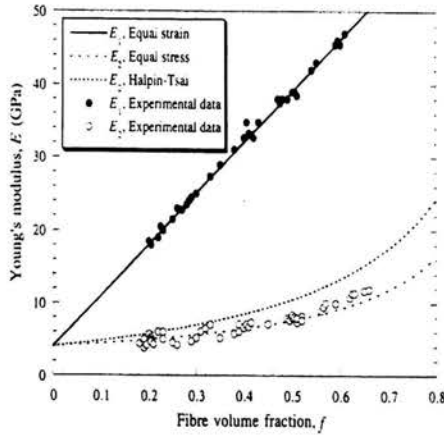


FIGURE 12. Comparison between experimental data for the axial and transverse moduli and corresponding predictions.

Beyond these simple models for predicting the transverse modulus, there are powerful but complex analytical tools as the Eshelby equivalent inclusion method (see Sec. 3) and numerical techniques as finite element method. The plots shown in Fig. 13 give an idea of the errors likely to be introduced in real cases using

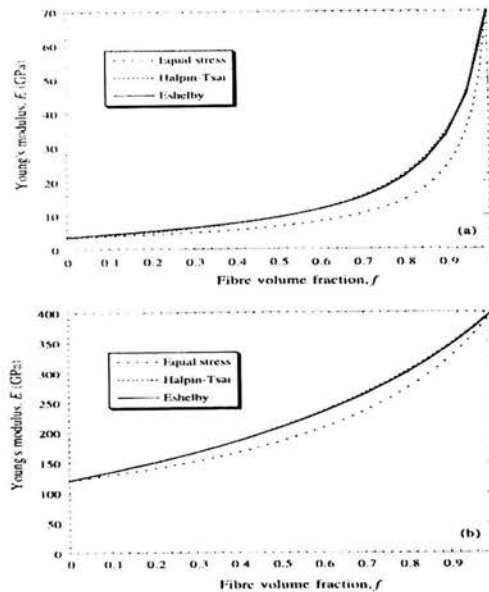


FIGURE 13. The transverse Young's modulus for (a) glass fibres in epoxy and (b) silicon carbide fibres in titanium.

simple analytical expressions as compared with the Eshelby method, which should be more reliable. It can be seen that the equal stress assumption gives a significant underestimate, whereas the Halpin-Tsai equation is quite reliable.

2.1.3. Shear stiffness. The shear moduli of composites can be predicted by evaluating the net shear strain induced when a shear stress is applied to the composite, in terms of the individual displacement contributions from the two constituents.

A shear stress designated τ_{ij} ($i \neq j$) refers to stress acting in the i -direction on the plane with a normal in the j -direction. Similarly, a shear strain γ_{ij} is a rotation towards the i -direction of the j -axis. The shear modulus G_{ij} is the ratio of τ_{ij} to γ_{ij} . As the composite body is not rotating, the condition $\tau_{ij} = \tau_{ji}$ must hold. In addition, $G_{ij} = G_{ji}$ so that $\gamma_{ij} = \gamma_{ji}$. Since the 2- and 3-directions are equivalent in the aligned fibre composite, it follows that there are two shear moduli, because $G_{12} = G_{21} = G_{13} = G_{31} \neq G_{23} = G_{32}$.

There are also two shear moduli for the slab model (Fig. 14), but these are unlikely to correspond closely with the values for the fibre composite.

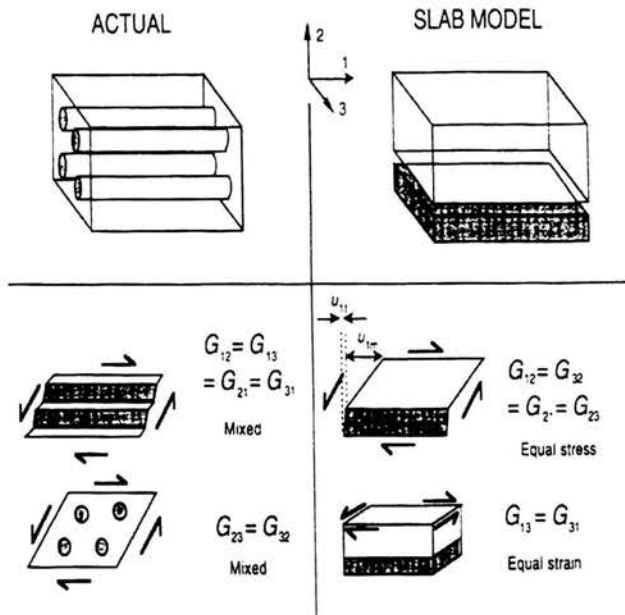


FIGURE 14. Schematic illustration of how the shear moduli are defined for a real fibre composite and for the slab model.

The stresses τ_{12} and τ_{21} are assumed to operate equally within both of the constituents. The derivation is similar to the equal stress treatment

$$\tau_{12} = \tau_{12f} = \gamma_{12f} G_f = \tau_{12m} = \gamma_{12m} G_m,$$

where γ_{12f} and γ_{12m} are the individual shear strains in the two constituents. The total shear strain is found by summing the two contributions to the total shear displacement in the 1-direction

$$\gamma_{12} = \frac{(u_{1f} + u_{1m})}{f + (1-f)} = f\gamma_{12f} + (1-f)\gamma_{12m}$$

and

$$G_{12} = \frac{\tau_{12}}{\gamma_{12}} = \frac{\tau_{12f}}{f\gamma_{12f} + (1-f)\gamma_{12m}} = \left[\frac{f}{G_f} + \frac{(1-f)\gamma_{12m}}{\tau_{12f}} \right]^{-1}$$

i.e.

$$G_{12} = \left[\frac{f}{G_f} + \frac{(1-f)}{G_m} \right]^{-1}. \quad (2.8)$$

The other shear modulus shown by the slab model $G_{13} = G_{31}$ in Fig. 14 corresponds to an equal shear strain condition and is analogous to the axial tensile modulus case. Then

$$G_{13} = fG_f + (1-f)G_m. \quad (2.9)$$

It may be noted that neither the equal stress condition nor the equal strain condition is close to the situation during shearing of the composite, in which the strain partitions unevenly within the matrix. Therefore neither of the above equations is expected to be very reliable, particularly the equal strain expression.

It is not obvious just how poor the approximation represented by Eq. (2.8) is likely to be, nor even which of the two actual shear moduli it will approach more closely. More rigorous methods predict that the values of G_{12} and G_{23} are rather close to each other, with G_{12} slightly larger in magnitude. Equation (2.8) gives a significant underestimate relative to both of them, while Eq. (2.9) is a gross overestimate. In view of this, the Halpin-Tsai equation is frequently employed. In this case, the appropriate equation is

$$G_{12} = \frac{G_m(1 + \xi\eta f)}{(1 - \eta f)}, \quad (2.10)$$

in which

$$\eta = \frac{\left(\frac{G_f}{G_m} - 1\right)}{\left(\frac{G_f}{G_m} + \xi\right)},$$

and the parameter ξ is again taken to have value of around unity. This has been done for the curves in Fig. 15, which shows comparisons between predictions of Eq. (2.10) and those of the equal stress (Eq. 2.8) and Eshelby models for both polymer and metal matrix composites. It can be seen that the Halpin-Tsai expression represent a fairly good approximation to the axial shear modulus (G_{12}). A striking feature of both the transverse and the shear moduli for polymer composites (Fig. 13a and 15a) is that they are close to the matrix values ($f = 0$) to the relatively high volume fractions ($f = 0.3-0.4$), although in both cases the true modulus is not as low as the prediction of the equal stress model.

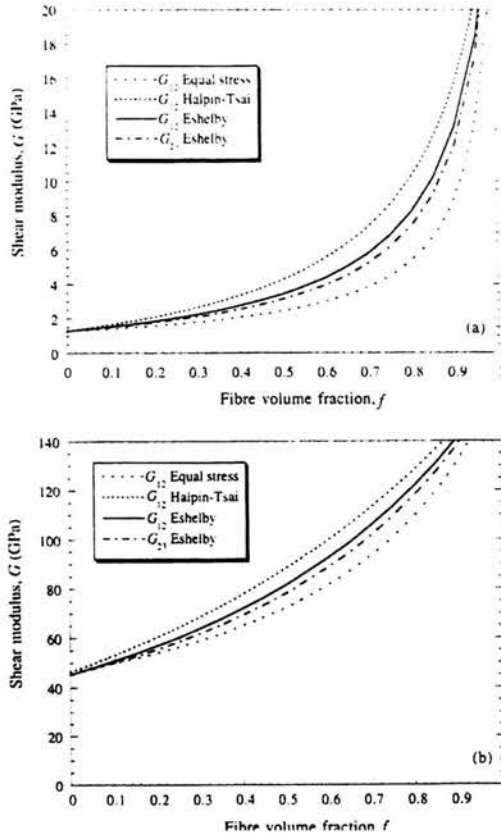


FIGURE 15. Predicted shear moduli for (a) glass fibres in epoxy and (b) silicon carbide fibres in titanium.

2.1.4. Poisson contraction effects. For an aligned fibre composite there are three different Poisson's ratios as illustrated in Fig. 16. This brings the total number of elastic constants identified for this material to seven.

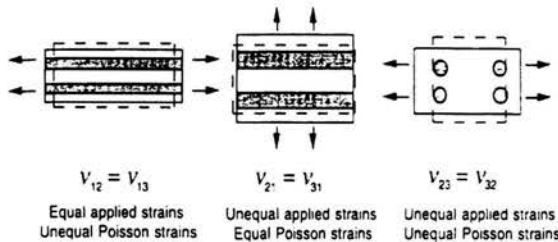


FIGURE 16. Schematic illustration of how three Poisson's ratios are defined.

However, because some of these constants are inter-related only five independent values are needed to describe the behaviour of such a transversely isotropic material. The following two relationships between identified constants account for this

$$\frac{\nu_{12}}{E_1} = \frac{\nu_{21}}{E_2} \quad \text{and} \quad G_{23} = \frac{E_2}{2(1-\nu_{23})}. \quad (2.11)$$

Estimation of three Poisson's ratios on the basis of the slab model presents difficulties because of the greater degree to which the contractions of the two constituents must match, when compared with the real composite. The effect of this is that although three Poisson's ratios can be identified for the slab model, a meaningful calculation can only be done for the equal imposed strain case giving ν_{12} . In this case, the Poisson strains for the two constituents can be valued independently and summed. Thus

$$\begin{aligned} \varepsilon_{2f} &= -\nu_f \varepsilon_{1f} = -\nu_f \frac{\sigma_{1f}}{E_f}, \\ \varepsilon_{2m} &= -\nu_m \varepsilon_{1m} = -\nu_m \frac{\sigma_{1m}}{E_m}, \end{aligned}$$

so that

$$\varepsilon_2 = - \left[\frac{f\nu_f\sigma_{1f}}{E_f} + \frac{(1-f)\nu_m\sigma_{1m}}{E_m} \right] = - [f\nu_f\varepsilon_1 + (1-f)\nu_m\varepsilon_1],$$

and

$$\nu_{12} = -\frac{\varepsilon_2}{\varepsilon_1} = f\nu_f + (1-f)\nu_m. \quad (2.12)$$

A simple rule of mixtures is therefore applicable, and because the equal strain assumption is accurate for axial stressing of the composite, this is expected to be a reliable prediction.

Simple expressions can also be derived to give fairly realistic predictions for the other two ratios. The ratio of the axial contraction to the transverse extension on stressing transversely, ν_{21} , is obtained from the reciprocal relationship given in Eq. (2.11), so that

$$\nu_{21} = [f\nu_f + (1-f)\nu_m] \frac{E_2}{E_1}. \quad (2.13)$$

This will be lower than ν_{12} because, on stressing transversely, the fibres will offer strong resistance to axial contraction. This leads to pronounced contraction in the other transverse direction, so that ν_{23} is expected to be high. An expression for ν_{23} may be obtained by considering the overall volume change experienced by the material

$$\Delta = \varepsilon_1 + \varepsilon_2 + \varepsilon_3 = \frac{\sigma_H}{K}, \quad (2.14)$$

in which σ_H is the applied hydrostatic stress and K is the bulk modulus of the composite. Only a single stress, σ_2 is being applied here, so that

$$\sigma_H = \frac{\sigma_1 + \sigma_2 + \sigma_3}{3} = \frac{\sigma_2}{3}.$$

Thus

$$\varepsilon_3 = \frac{\sigma_2}{3K} - \varepsilon_1 - \varepsilon_2, \quad (2.15)$$

which leads directly to

$$\nu_{23} = -\frac{\varepsilon_3}{\varepsilon_2} = -\frac{\sigma_2}{3K\varepsilon_2} + \frac{\varepsilon_1}{\varepsilon_2} + 1$$

i.e.

$$\nu_{23} = 1 - \nu_{21} - \frac{E_2}{3K}. \quad (2.16)$$

The bulk modulus of the composite can be estimated via an equal stress assumption, so that

$$\sigma_H = \Delta_f K_f = \Delta_m K_m$$

and

$$\Delta = f\Delta_f + (1-f)\Delta_m$$

giving

$$K = \frac{\sigma_H}{\Delta} = \left[\frac{f}{K_f} + \frac{(1-f)}{K_m} \right]^{-1}. \quad (2.17)$$

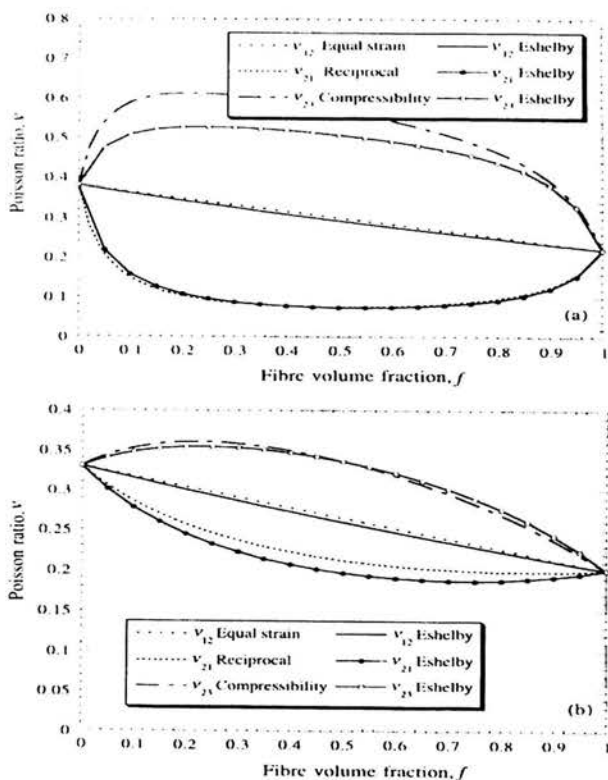


FIGURE 17. Predicted Poisson's ratios for (a) glass fibres in epoxy and (b) silicon carbide fibres in titanium.

The bulk moduli of the constituents are related to other elastic constants by expressions such as

$$K_f = \frac{E_f}{3(1 - 2\nu_f)}$$

The accuracy of Eq. (2.16) is determined largely by the error in E_2 . In the comparison shown in Fig. 17, the Halpin-Tsai values of E_2 predicted by Eq. (2.7) were used in obtaining values for ν_{21} and ν_{23} . It can be seen that agreement with the Eshelby method is fairly good. These plots convey an idea of the pronounced tendency under transverse loading for the composite to contract in the other transverse direction in preference to the axial direction.

2.2. The shear lag model

The preparation of composites containing short fibres or equiaxed particles allows scope for using a wider range of reinforcement and more versatile processing and forming routes. Thus, there is interest in understanding the distribution of stresses within such a composite and the consequences of this for the stiffness and other mechanical properties.

The most widely used model describing the effect of loading in aligned short-fibre composite is the shear lag model, which centres on the transfer of tensile stress from matrix to fibre by means of interfacial shear stresses. The basis of the calculations is shown schematically in Fig. 18. In this diagram, reference lines are drawn on a fibre and the surrounding matrix, which are initially straight and normal to the

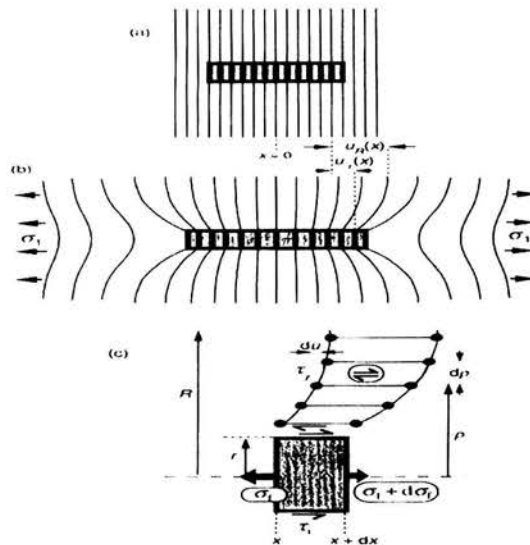


FIGURE 18. The shear lag model showing: (a) unstressed system, (b) axial displacements u introduced on applying tension parallel to the fibre and (c) variation with radial location of the shear stress and strain in the matrix.

fibre axis. External loading is then applied, Fig. 18b, parallel to the fibre axis. The reference lines distort in the manner shown. Attention is concentrated on the shear distortions of the matrix close to the fibre, represented schematically in Fig. 18. The model is based on considering the shear stresses in the matrix and at the interface.

2.2.1. Stress and strain distributions. The radial variation of shear stress in the matrix τ (at a given axial distance x from the fibre mid-point) is obtained by equating the shear forces on neighbouring annuli with radii r_1 , r_2 of length dx (see Fig. 18c)

$$2\pi r_1 \tau_1 dx = 2\pi r_2 \tau_2 dx$$

or

$$\frac{\tau_1}{\tau_2} = \frac{r_2}{r_1}.$$

The shear stress τ in the matrix at any radius ρ is therefore related to that of the fibre/matrix interface (radius r), τ_i by

$$\tau = \tau_i \left(\frac{r}{\rho} \right).$$

The strain field around the fibre can be defined in terms of the displacement u of the matrix in the x -direction, relative to the position for no applied stress (see Fig. 18). The increment of this displacement, du , on moving out from the fibre axis by $d\rho$, is determined by the shear strain γ , and hence by the shear modulus G_m

$$\frac{du}{d\rho} = \gamma = \frac{\tau}{G_m} = \frac{\tau_i}{G_m} \left(\frac{r}{\rho} \right).$$

For any given value of x , the difference between the displacement of the matrix at a radius R and that of the interface is given by a simple integration

$$\int_{u_r}^{u_R} du = \frac{\tau_i r}{G_m} \int_r^R \frac{d\rho}{\rho}$$

i.e.

$$u_R - u_r = \frac{\tau_i r}{G_m} \ln \left(\frac{R}{r} \right). \quad (2.18)$$

The matrix strain is assumed to be uniform remote from the immediate vicinity of the fibre. The radius R represents some far-field location where this condition becomes operative. In a composite containing an array of fibres the appropriate value of R/r is related to the proximity of neighbouring fibres and hence to the fibre volume fraction f . The exact relationship between R/r and f is dependent on the way the fibres are arranged; however, because R/r appears in a logarithmic term, the final result is relatively insensitive to the details of the fibre arrangement. A hexagonal array of fibres leads to

$$f = \frac{\pi r^2}{(2R)(R\sqrt{3})},$$

$$\left(\frac{R}{r}\right)^2 = \frac{\pi}{2f\sqrt{3}} \frac{1}{f}. \quad (2.19)$$

The build up of tensile stress in the fibre σ_f is determined from the distribution of interfacial shear stress. Referring to Fig. 18c, the basic force balance acting on an element of the fibre is

$$2\pi r dx \tau_i = -\tau r^2 d\sigma_f, \\ \frac{d\sigma_f}{dx} = -\frac{2\tau_i}{r}. \quad (2.20)$$

Now, the variation of τ_i with x is unknown a priori, but Eq. (2.18) can be used to relate it to displacements and hence to axial strains. It is assumed that there is no shear strain in the fibre and the interfacial adhesion is perfect (so that $u_r = u_f$, the displacement of the fibre surface).

The following relationship is used for the shear modulus of the matrix

$$G_m = \frac{E_m}{2(1 + \nu_m)},$$

and substitution in Eq. (2.18) leads to the result

$$\frac{d\sigma_f}{dx} = -\frac{2E_m(u_R - u_f)}{(1 + \nu_m)r^2 \ln(1/f)}. \quad (2.21)$$

The displacements themselves are unknown, but their differentials are related to identifiable strains. For the fibre

$$\frac{du_f}{dx} = \epsilon_f = \frac{\sigma_f}{E_f}. \quad (2.22)$$

The corresponding expression for the matrix is less well defined. The differential of u_R will approximate to the far-field matrix strain, at least over most of the length of the fibre, and this, in turn, is close to the overall composite strain ϵ_1

$$\frac{du_R}{dx} \approx \epsilon_m = \epsilon_1. \quad (2.23)$$

Although not rigorous, this represents a fairly good approximation; the far-field matrix strain is shown in Fig. 18b as being approximately uniform along (and beyond) the length of the fibre. The fibre strain (and stress) builds up with distance from ends of the fibre.

Finally, the stress distribution in the fibre can be determined. Differentiation of Eq. (2.21) and substitution leads to

$$\frac{d^2\sigma_f}{dx^2} = \frac{n^2}{r^2}(\sigma_f - E_f \epsilon_1), \quad (2.24)$$

in which n is a dimensionless constant given by

$$n = \left[\frac{2E_m}{E_f(1 + \nu_m) \ln(1/f)} \right]^{\frac{1}{2}}. \quad (2.25)$$

Equation (2.24) is a standard second-order linear differential equation with the solution

$$\sigma_f = E_f \varepsilon_1 + B \sinh\left(\frac{nx}{r}\right) + D \cosh\left(\frac{nx}{r}\right). \quad (2.26)$$

On applying the boundary conditions

$$\sigma_f = 0 \quad \text{at} \quad x = \pm L,$$

where L is the fibre half-length, and writing the fibre aspect ratio L/r as s , this gives the solution

$$\sigma_f = E_f \varepsilon_f \left[1 - \cosh\left(\frac{nx}{r}\right) \operatorname{sech}(ns) \right]. \quad (2.27)$$

The variation of interfacial shear stress along the fibre length is derived, according to Eq. (2.20), by differentiating this equation, to give

$$\tau_i = \frac{n \varepsilon_1}{2} E_f \sinh\left(\frac{nx}{r}\right) \operatorname{sech}(ns). \quad (2.28)$$

2.2.2. The stress transfer length. Equations (2.27) and (2.28) allow predictions to be made about the stress distribution along the length of the fibre. An example is shown in Fig. 19.

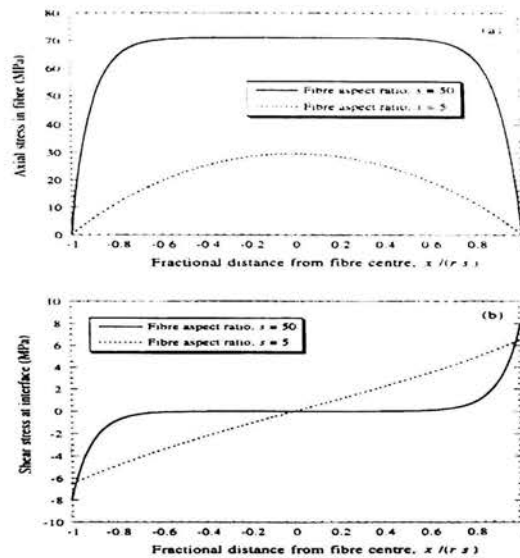


FIGURE 19. Predicted variations in (a) fibre tensile stress and (b) interfacial shear stress along the length of a glass fibre in polyester/30% glass fibre composite subjected to an axial strain of 10^{-3} .

This shows the variations in fibre tensile stress and interfacial shear stress along the length of a fibre in a composite of aligned glass fibres in a polyester resin matrix. The tensile stress is zero at the fibre ends and a maximum in the centre.

The interfacial shear stress is zero in the centre and a maximum at the ends. For the high aspect ratio case ($s = 50$), the fibre is long enough for the tensile stress to build up until the fibre has a strain equal to that of the matrix and the composite. This gives rise to the plateau region of the fibre stress curve and a region of zero interfacial shear stress. (With continuous aligned fibres, all of the composite is in this equal strain condition with respect to stress in the axial direction – see previous subsection). There are regions of the fibre near the ends which are less heavily stressed than this central plateau region, so that the average fibre stress is lower than in a long-fibre composite subjected to the same external load. The reinforcing efficiency decreases as the fibre length is reduced, since this increases the proportion of the total fibre length which is not fully loaded. This behaviour leads to the concept of a stress transfer length, over which the strain in the fibre builds up to the plateau (matrix) value. For the case shown, this length is about 10 fibre diameters. Provided that the system remains fully elastic and there is no interfacial sliding, this value is dependent only on the elastic constants of fibre and matrix. (With a stiffer matrix such as metal, the stress transfer length will be shorter as a result of higher interfacial shear stresses).

For the low aspect ratio ($s = 5$) case, the whole length of the fibre is only 5 fibre diameters so that the stress in it does not build up to a plateau value. Such fibres are not providing very efficient reinforcement, because they carry much less stress than would longer fibres in the same system. A stress transfer aspect ratio s_t can be identified as the one exhibited by fibres in which the peak (central) stress closely approaches the maximum possible (at which its strain is equal to the value being imposed on the composite). From Eq. (2.27), this will be the case when

$$\cosh(0) \operatorname{sech}(ns) \gg 1.$$

Since $\cosh(0) = 1$, the requirement is to set $\operatorname{sech}(ns) (= 1/\cosh(ns))$ to a suitably low value. Choosing 0.1, the condition becomes

$$\cosh(ns) = 10 \quad \text{i.e.} \quad s_t \approx \frac{3}{n}. \quad (2.29)$$

The value of n , obtained from Eq. (2.25) becomes smaller as the fibre/matrix modulus ratio rises, and as the volume fraction of fibres decreases. In general, however, the value does not vary widely; it is typically about 0.1 for polymer matrix composites and 0.4 for metal matrix composites. The corresponding values of s_t are therefore of the order of 30 and 7, respectively. (For ceramic matrix composites, the value of n is normally close to unity and hence s_t is small. However, the introduction of ceramic fibres into a ceramic matrix is normally done for purposes other than that of stiffening the material, namely for the increased toughening, so that efficient load transfer is not a primary objective).

The shear lag model provides qualitatively realistic results. For example, the finite difference method illustrates how high matrix shear strains near the end of the fibre lead to a build-up of fibre tensile strain, Fig. 20. However, quantitative examination reveals discrepancies. The data in Fig. 21 were obtained by measuring the local tensile strain at different points along a polydiacetylene fibre embedded in an epoxy matrix subjected to an external tensile load. While the general appearance

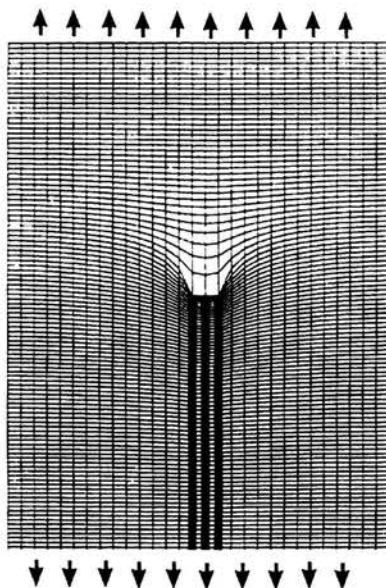


FIGURE 20. An elastic deformation map obtained by a finite difference method showing how initially orthogonal grid around a fibre end becomes distorted on applying an axial tensile stress. (The fibre/matrix stiffness ratio = 40).

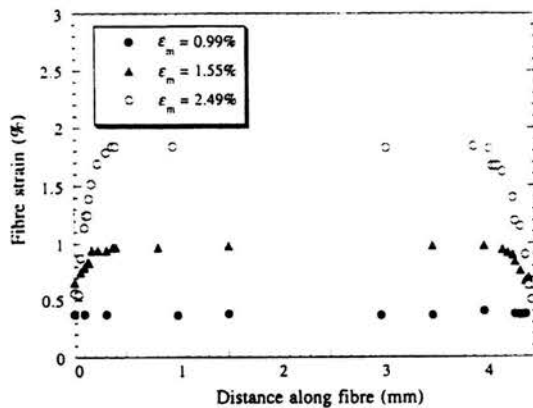


FIGURE 21. Strains in a polydiacetylene fibre embedded in an epoxy matrix, measured by shifts in the Raman resonance spectrum for three values of the macroscopic strain applied to the matrix. The fibre aspect ratio was about 200 and the fibre/matrix stiffness ratio was about 16.

of the curves agrees well with the shear lag model for the higher imposed strains, there are discrepancies. Notable among these is the fact that the fibre stress does not fall to zero at the ends. This is primarily the result of the transfer of tensile stress across the fibre ends which is neglected in the basic model and is relatively unimportant in composites with high fibre aspect ratio.

2.2.3. Transfer of normal stress across fibre ends. Any attempt to account for this effect, while retaining the attractive simplicity of the shear lag model, must involve postulating an analytical expression for the fibre end stress σ_e . This must be an arbitrary postulate, since there is no scope within the shear lag framework for any rigorous description of stresses beyond the fibre end. It is suggested that σ_e be set equal to the average of the peak fibre stress and the remote matrix stress values predicted by the standard shear lag model

$$\sigma_e = \frac{\sigma_{f0} + \sigma_{m0}}{2},$$

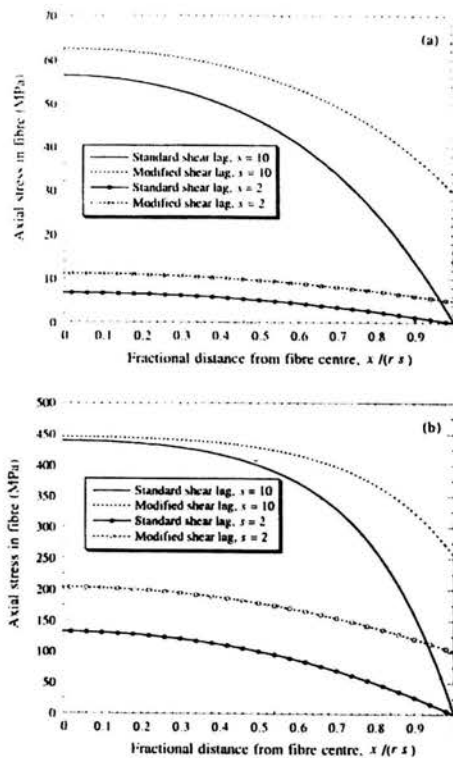


FIGURE 22. Predicted variations in axial stress within (a) a glass fibre in a polyester/30% glass fibre composite and (b) a SiC fibre in Al 30% SiC fibre composite; at a composite strain of 10^{-3} .

in which σ_{f0} is given by substituting $x = 0$ in Eq. (2.27) and σ_{m0} is taken as $E_m \varepsilon_1$ (matrix average stress). This leads to an expression for σ_e

$$\sigma_e = \frac{1}{2} \varepsilon_1 \left[E_f (1 - \operatorname{sech}(ns)) + E_m \right] = \varepsilon_1 E_m'' \quad (2.30)$$

and hence, using the new boundary conditions $\sigma_f = \sigma_e$ at $x = \pm L$ to solve Eq. (2.26), a new expression is obtained for σ_f :

$$\sigma_f = \varepsilon_1 \left[E_f - (E_f - E_m) \cosh\left(\frac{\pi x}{r}\right) \operatorname{sech}(ns) \right]. \quad (2.31)$$

In Fig. 22 predictions from this equation are compared with those of the standard model (Eq. 2.27) for polymer- and metal matrix composites. The predicted stresses in the fibre are significantly higher for the modified model, particularly near the fibre ends. Taking account of fibre end stress transfer naturally leads to the fibres carrying more load, particularly for short fibres. This results in an increase in the predicted stiffness of the composite.

2.2.4. Prediction of stiffness. The basic results of the shear lag model can be used to predict the elastic deformation of the composite. Consider a section of area A taken normal to the loading direction, as shown in Fig. 23. This section intersects individual fibres at random positions along their length. The applied load can be expressed in terms of the contributions from the two components

$$\sigma_1 A = f A \bar{\sigma}_f + (1 - f) A \bar{\sigma}_m$$

or

$$\sigma_1 = f \bar{\sigma}_f + (1 - f) \bar{\sigma}_m, \quad (2.32)$$

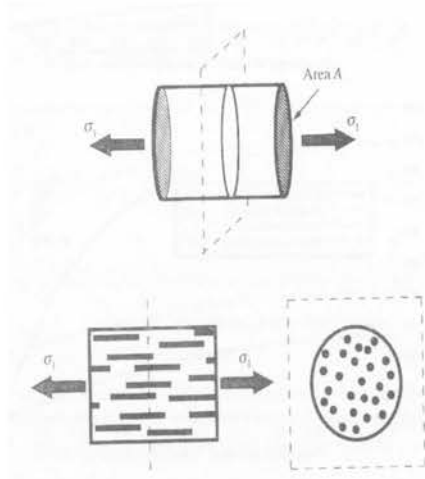


FIGURE 23. Random section through a stressed short-fibre composite.

in which $\bar{\sigma}_f$ and $\bar{\sigma}_m$ are the volume-average stress carried by fibre and matrix. This equation is often termed the “Rule of Averages” (see next section). The average fibre stress is evaluated from Eq. (2.27)

$$\bar{\sigma}_f = \frac{E_f \varepsilon_1}{L} \int_0^L \left[1 - \frac{\cosh\left(\frac{nx}{r}\right)}{\cosh(ns)} \right] dx,$$

$$\bar{\sigma}_f = E_f \varepsilon_1 \left(1 - \frac{\tanh(ns)}{ns} \right). \tag{2.33}$$

For the matrix, it is again conventional to resort to the assumption of a uniform tensile strain equal to that imposed on the composite

$$\bar{\sigma}_m \approx E_m \varepsilon_1. \tag{2.34}$$

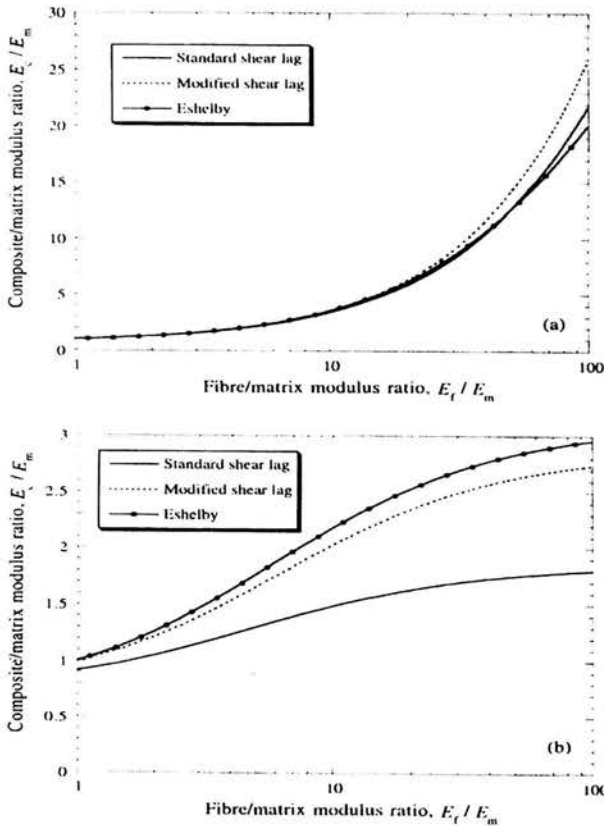


FIGURE 24. Predicted composite/matrix modulus ratio as a function of the fibre matrix modulus ratio, for composites with 30% reinforcement and fibre aspect ratio of (a) 30 and (b) 3.

Combining Eqs. (2.32)-(2.34) gives the stress-strain relationship for the composite

$$\sigma_1 = \varepsilon_1 \left[f E_f \left(1 - \frac{\tanh(ns)}{ns} \right) + (1 - f) E_m \right]. \quad (2.35)$$

The same procedure for the modified model, taking account of fibre end stress transfer, leads to

$$\sigma_1 = \left[f E_f \left(1 - \frac{E_f - E_m'' \tanh(ns)}{E_f n s} \right) + (1 - f) E_m \right] \varepsilon_1. \quad (2.36)$$

These equations can be tested by making comparisons with prediction from more rigorous Eshelby model, Fig. 24.

It can be seen that the standard shear lag model is inaccurate for low fibre aspect ratios. The predictions of the standard model look particularly unreliable when the fibre/matrix modulus ratio is small. This suggests that the fibre end stress modification might be particularly useful for discontinuously reinforced metal matrix composites. This is confirmed by the data in Fig. 25, which compares predictions from three models with measured stiffness for particulate metal matrix composite. The standard shear lag model is clearly unsuitable for such materials.

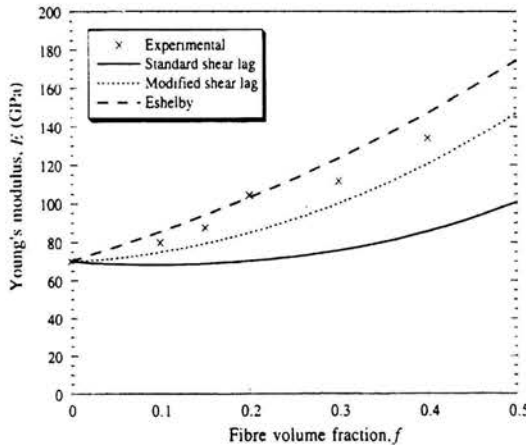


FIGURE 25. Comparison between experimental data and model predictions for the stiffness of Al/SiC particulate composites produced by extrusion. As the particles are not equiaxed, and tend to become aligned during processing, an aspect ratio of 2 was used in the predictions.

It may be noted from Eqs. (2.35) and (2.36) that the stiffness approaches the limiting (Rule of Mixture) value as s becomes large enough for $\tanh(ns)/ns$ to become negligible. Since $\tanh(ns)/ns \sim 1$ for $ns \geq 3$ and assuming that 0.1 can be taken as $\ll 1$,

$$s_{RM} \approx \frac{10}{n},$$

in which s_{RM} is the fibre aspect ratio needed for the composite modulus to approach its maximum (Rule of Mixtures) value. As noted earlier, values of n are typically around 0.1 for polymer composites and 0.4 for metal matrix composites. This suggests values for s_{RM} of about 100 and 25 for polymer- and metal-based composites, respectively. These can be regarded as target (minimum) aspect ratios when the main objective is to maximise the load transfer and hence the stiffness.

2.2.5. Onset of inelastic behaviour. Several phenomena can occur which cause departure from ideal elastic behaviour. These include plastic deformation of the matrix, debonding and subsequent frictional sliding at the interface, formation of cavities or cracks in the matrix (particularly at fibre ends) and fracture of fibres. These effects change the stress distribution and hence affect the stress-strain curve. They are also related to the onset of failure and hence to the strength of the material. Description and analysis of these important micromechanisms are beyond the scope of this course. Nevertheless, it is appropriate to examine a simple extension to the basic shear lag theory designated to predict the onset of departure from elastic behaviour.

The onset of matrix plasticity or interfacial sliding is expected to occur at the fibre ends where the matrix shear stress is a maximum. A critical interfacial shear stress τ_{cr} can be specified for these processes. Substitution of τ_{cr} into Eq. (2.28), with $x = L$, gives the composite strain at the onset of such inelastic behaviour

$$\varepsilon_{1cr} = \frac{2\tau_{cr} \coth(ns)}{n E_f}. \quad (2.37)$$

This can be converted to an applied stress using Eq. (2.35), leading to the expression

$$\sigma_{1cr} = \frac{2\tau_{cr}}{n E_f} \left\{ [f E_f + (1 - f) E_m] \coth(ns) - \frac{f E_f}{ns} \right\}. \quad (2.38)$$

This point does not correspond to a clearly identifiable composite yield stress, since yielding (or interfacial sliding) is only taking place in a small localized region. However, at this point the stress-strain curve will start to depart from a linear plot. As an illustration of the use of Eq. (2.37), in a typical glass fibre reinforced polymer composite, with $\tau_{cr} = 20$ MPa, the composite strain at the onset of inelastic behaviour is about 0.6% for long fibres ($s \sim 30$) and about 0.3% for short fibres ($s \sim 5$).

The likelihood of fibre fracture taking place before matrix yielding or interfacial sliding can also be examined. The peak stress in the fibre at the onset of interfacial sliding or yielding is found from Eq. (2.27) by setting $x = 0$ and the composite strain to the value given by Eq. (2.37). This leads to

$$\sigma_{f0} = \frac{2\tau_{cr}}{n} [\coth(ns) - \operatorname{cosech}(ns)]. \quad (2.39)$$

Schematic plots of this relationship are shown in Fig. 26 which also gives an indication of the range of values expected for τ_{cr} in metallic and polymeric matrices and for the fracture stress σ_{cr} exhibited by ceramic fibres. It is clear from this plot that

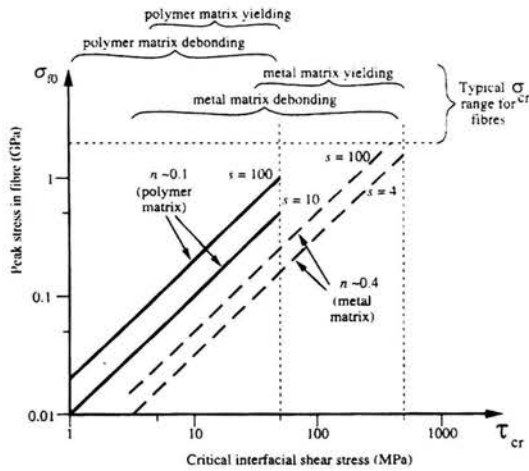


FIGURE 26. Plots of the dependence of peak fibre stress σ_{f0} (at the onset of interfacial sliding or matrix yielding) on the critical shear stress for the onset of these phenomena τ_{cr} according to Eq. (2.39).

on increasing the load applied to either type of composite, yielding or sliding at the interface takes place before fibres start to fracture.

As the composite strain is increased, yielding (or sliding) spreads along the length of the fibre, raising the tensile stress in the fibre as the interfacial shear stress increases. Fracture of fibres may then become possible, and a simple treatment can be used to explore the limit of this effect. If it is assumed that the interfacial shear stress becomes uniform at τ_{cr} along the length of the fibre, then a critical aspect ratio s_{cr} can be identified below which the fibre cannot undergo any further fracture. This corresponds to the peak (central) fibre stress just attaining its ultimate strength σ_{cr} so that integration of Eq. (2.20) along the fibre half-length leads to

$$s_{cr} = \frac{\sigma_{cr}}{2\tau_{cr}}.$$

The consequence is that a distribution of aspect ratios between s_{cr} and $s_{cr}/2$ is expected, if the composite is subjected to a large strain. The value of s_{cr} ranges from over 100 for a polymer composite with poor interfacial bonding to about 2-3 for a strong metallic matrix.

3. Overall properties – advanced models

Continuum mechanics deals with idealized materials consisting of material points and material neighbourhoods. It assumes that the material distribution, the stresses, and the strains within an infinitesimal material neighbourhood of a typical particle (or a material element) can be regarded as essentially uniform. On the microscale, however, the infinitesimal material neighbourhood, in general, is not uniform, consisting of various constituents with differing properties and shapes, i.e. an infinitesi-

mal material element has its own complex and, in general, evolving microstructure. Hence, the stress and strain fields within the material element likewise are not uniform at the microscale level. One of the main objectives of micromechanics is to express in a systematic and rigorous manner the *continuum quantities* associated with an infinitesimal material neighbourhood in terms of the parameters that characterize the *microstructure and properties of the microconstituents* of the material neighbourhood.

3.1. Representative volume element

A representative volume element (RVE) of a material point of a continuum mass is a material volume which is statistically representative of the infinitesimal material neighbourhood of that material point. The continuum material point is called a macro-element. The corresponding microconstituents of the RVE are called the micro-elements. An RVE must include a very large number of micro-elements, and be statistically representative of the local continuum properties.

Figure 27a shows a continuum, and identifies a typical material point P surrounded by an infinitesimal material element. When the macro-element is magnified, as sketched in Fig. 27b, it may have its own complex microstructure. It may consist of grains, separated by grain boundaries, voids, inclusions, cracks, and other similar defects. To be representative, this RVE must include a very large number of such microheterogeneities. Figure 28 shows the microstructure in Al-Si/SiC particles metal matrix composites processed by investment cast (slow cooling, Fig. 28a) and the pressure die cast (rapid cooling, Fig. 28b). At the slower cooling rate, it is clear that the SiC particles have been pushed into the interdendritic regions by the growing dendrites, causing severe clustering. For the more rapid cooling it seems likely that the growing dendrites have at least partially engulfed the particles so that less pushing has occurred; in any event, because the scale of the dendrite arm spacing is similar to that of a typical particle diameter, pushing can only occur over short distances and does not lead to pronounced clustering.

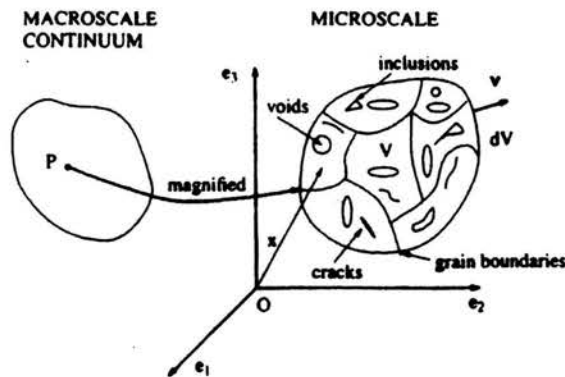


FIGURE 27. Representative volume element.

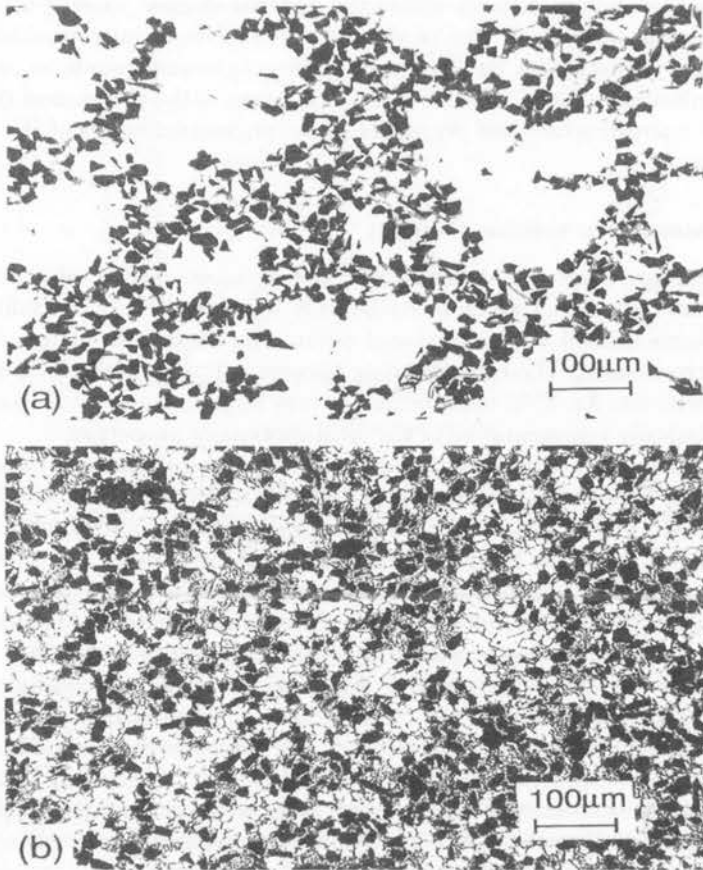


FIGURE 28. Optical micrograph of Al-Si/SiC composite; (a) slow cooling and (b) rapid cooling.

Figures 29 are optical micrographs of a metal-matrix composite with particulates, Fig. 29a,b, and short fibres, Fig. 29c. Formation of ceramic-rich bands during extrusion is clear. The asymmetry of the ceramic content distribution on either side of the band, apparent in Fig. 29c, can be explained in terms of superimposed gradients of temperature and strain rate across the section of the extrudate. A mechanism involves ceramic particles migration down a gradient of matrix flow stress associated with a thermal gradient caused by the strain localization. Fibres appear to be more prone to the effect than particles, possibly because they rotate, and hence interact more with each other, during the process.

In these examples, a sample of typical dimension of one millimetre may be used as an RVE. As may be inferred from these illustrations, to quantify the concept of an RVE, two length-scales are necessary; one is the continuum or macro-length scale, by which the infinitesimal material neighbourhood is measured; the second is the micro-length-scale which corresponds to the smallest microconstituent whose

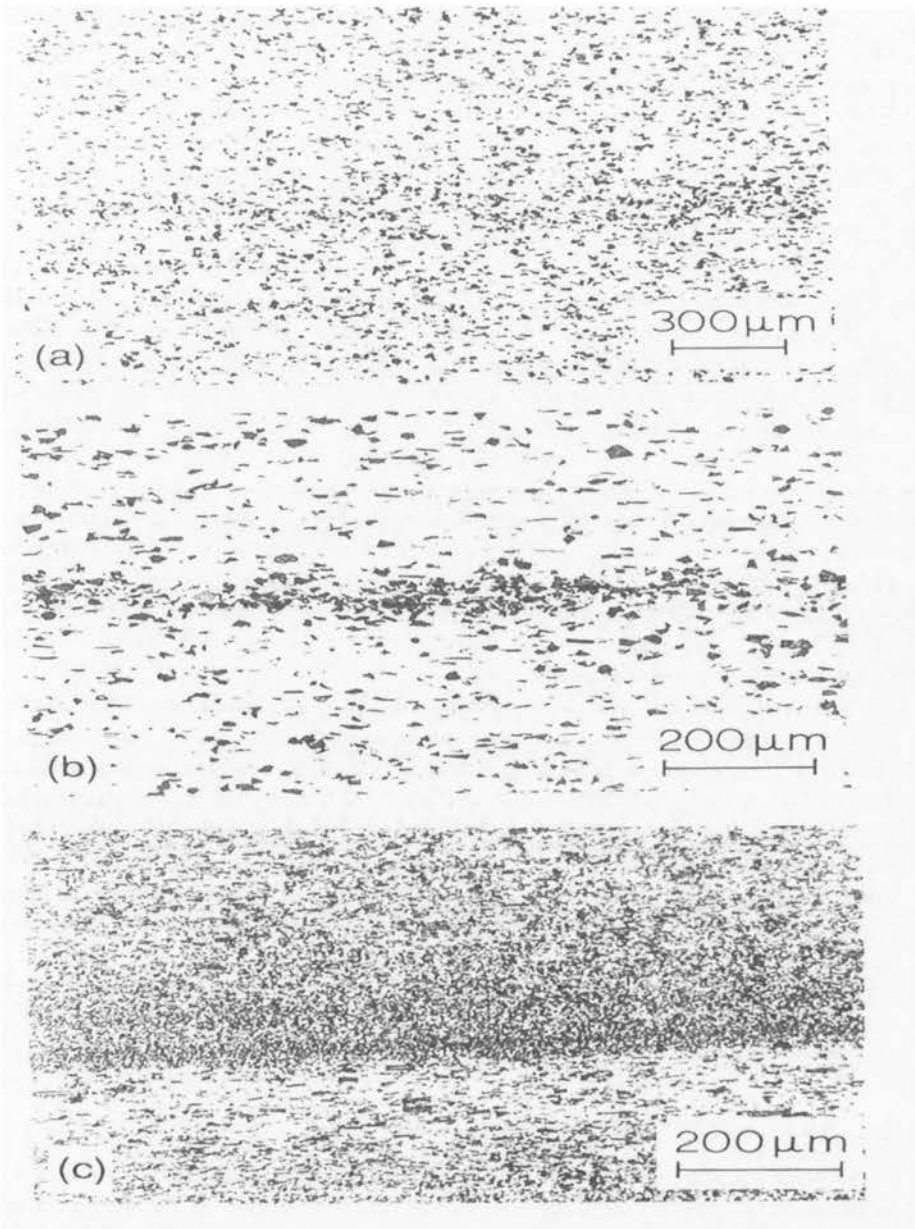


FIGURE 29. Formation of ceramic-rich bands during extrusion; (a) slight or (b) moderate banding in particulate (SiC) composite, and (c) severe banding in short fibre reinforced metal matrix composite.

properties and shape are judged to have direct, first-order effects on the overall response and properties of the continuum. In general, the typical dimension of the macro-element, D , must be orders of magnitude larger than the typical dimension of the micro-element, d ; i.e. $D/d \gg 1$. For example, if the continuum is a polycrystalline solid which is viewed as a homogenized continuum, and one is interested in describing the aggregate or polycrystal properties (the polycrystal being the macro-element) in terms of single-crystal properties (each crystal being a micro-element), then the dimension, D , of the RVE should be much larger than the typical size, d , of the individual crystals. As a second example, if one is interested in estimating the elastic moduli of a whisker reinforced composite in terms of the matrix (assumed uniform and homogeneous) and the whisker parameters, then the size of the RVE must be so that it includes a large number of whiskers. In either example, whether or not the micro-elements have a random, periodic, or other distribution does not affect the requirements of $D/d \gg 1$, although, of course, the corresponding overall properties of the RVE are directly affected by this distribution. Note that the absolute dimensions of the microconstituents may be very large or very small, depending on the size of the continuum mass and the objectives of the analysis. It is only the relative dimensions that are of concern. For example, in characterizing the overall properties of a mass of compacted fine powder in powder-metallurgy, with grains of submicron size, a neighbourhood of a dimension of 100 microns would be sufficient as an RVE, whereas in characterizing an earth dam as a continuum, with aggregates of many centimetres in size, the absolute dimension of an RVE would be of the order of tens of meters.

Another important question is what constitutes an underlying essential micro-constituent. This is also a relative concept depending on the particular problem and the particular objective. It must be addressed through systematic microstructural observation at the level of interest, and must be guided by experimental results. Perhaps one of the most vital decisions is the definition of the RVE. An optimum choice would be one that includes the most dominant features that have first-order influence on the overall properties of interest, and at the same time yields the simplest model. This can only be done through a coordinated sequence of microscopic (small-scale) and macroscopic (continuum-scale) observation, experimentation and analysis. In many problems in the mechanics of materials, suitable choices often emerge naturally in the course of the examination of the corresponding physical attributes and the experimental results.

3.2. The Eshelby equivalent inclusion method

Internal stresses are commonplace in almost any material which is mechanically inhomogeneous. Typically, their magnitude varies according to the degree of inhomogeneity for an externally loaded polycrystalline cubic metal, differently oriented crystallites will be stressed to different extents, but these differences are usually quite small. For a composite consisting of two distinct constituents with different stiffnesses, these disparities in stress will commonly be much larger. Internal stresses arise as a result of some kind of *misfit* between the shapes of the constituents (matrix and reinforcement, i.e. fibre, whisker or particle). Such a misfit could arise from a temperature change, but a closely related situation is created during mechanical

loading - when a stiff inclusion tends to deform less than the surrounding matrix. Analysis of the stress required to mate up the inclusion and matrix across the interface allows the prediction of properties such as thermal expansivity and stiffness. For an arbitrary inclusion shape, this analysis can only be carried out numerically, but for the special case of an ellipsoid an analytical technique can be employed. The key point here is that the ellipsoid, which can have any aspect ratio, has a uniform stress at all points within it. Figure 30 shows the slice from an axisymmetric three-dimensional photoelastic model containing a prolate ellipsoidal inclusion of stiffness ~ 2.5 times that of the matrix, viewed between crossed polars. The model was loaded in axial compression. The pattern of fringes (contours of equal principal stress difference) shows that the stress within the matrix fluctuates in a complicated manner, the stress being largest at the inclusion ends and smaller than the applied stress about the equator. The stress within the inclusion, on the other hand, is larger than the applied stress and is uniform throughout.

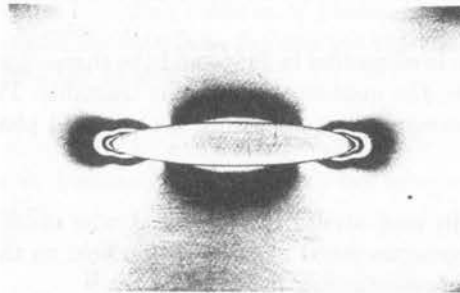


FIGURE 30. Photoelastic model of ellipsoidal inclusion loaded in axial compression.

The Eshelby technique is based on representing the actual inclusion by one made of matrix material which has an appropriate misfit strain so that the stress field is the same as for the actual inclusion. Suppose a region within a homogeneous medium was suddenly to transform in shape, so that it no longer fitted freely into the hole in the matrix from which it came; what would the stress field look like? The answer to this question would at first sight appear to have little to do with calculating the stresses within composites, but Eshelby showed that there is an elegant solution to this problem, which can be applied to a wide variety of other situations. The consequences of a spontaneous transformation of the type discussed above can best be visualized in terms of displacement maps, Fig. 31.

In these diagrams, the grid lines represent the displacement of an originally square mesh, while the thickness of lines represents the stiffness. A transformation (i.e. a shape change) imposed on a region within a matrix tends to cause complex distortions in both the transformed region and the surrounding matrix. This is so far non-uniform strains (in this case a linear change in width with height, Fig. 31a) and uniform strains (in this case a simple shear, Fig. 31b). It is clear that the elastic strain field is very complicated, both inside and outside the constrained transformed region, and for this reason an analytic solution is not usually possible. An example of such a spontaneous shape change is provided by a martensitic transformation. When

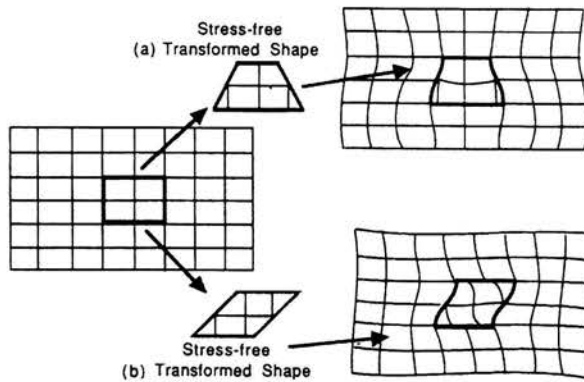


FIGURE 31. Schematic illustration of how a transformation imposed on a matrix region cause complex distortions for (a) non-uniform strains and (b) uniform strains.

the transformed region is ellipsoidal in shape and the shape change is a uniform one (i.e. ellipsoid), however, the mathematics become tractable. This is because under these conditions the stress and strain within the enclosed phase are uniform (see Fig. 30).

3.2.1. Average strain and stress theorems. Under conditions of an imposed macroscopically homogeneous stress or deformation field on the RVE, the average stress and strain are representatively defined by

$$\langle \varepsilon_{ij} \rangle = \frac{1}{V} \int_V \varepsilon_{ij} dV, \quad (3.1)$$

$$\langle \sigma_{ij} \rangle = \frac{1}{V} \int_V \sigma_{ij} dV, \quad (3.2)$$

where V is the volume of the RVE and the symbol $\langle \rangle$ denotes volume averaging. Homogeneous boundary conditions applied on the surface of a homogeneous body will produce a homogeneous field there. Such boundary conditions are obtained by imposing displacements at the boundary S in the form

$$u_i(S) = \varepsilon_{ij}^0 x_j, \quad (3.3)$$

where ε_{ij}^0 are constant strains. Alternatively, traction can be imposed on S so that

$$t_i = \sigma_{ij}^0 n_j, \quad (3.4)$$

where σ_{ij}^0 are constant stresses and \mathbf{n} is the unit outward normal vector to S .

To calculate the average strains in composite material it appears that one must solve the elasticity problem of the RVE subjected to the displacement homogeneous boundary conditions, Eq. (3.3). The strain-displacement relations are

$$\varepsilon_{ij} = \frac{1}{2}(u_{i,j} + u_{j,i}). \quad (3.5)$$

Substituting (3.5) in (3.2) yields

$$2V \langle \varepsilon_{ij} \rangle = \int_{V_1} (u_{i,j}^{(1)} + u_{j,i}^{(2)}) dV_1 + \int_{V_2} (u_{i,j}^{(2)} + u_{j,i}^{(1)}) dV_2. \tag{3.6}$$

where "1" and "2" denote phase 1 and 2 of the two phased composites with V_1, V_2 being the volumes occupied by the two phases. The use of Gauss theorem

$$\int_V u_{i,p} dV = \int_S u_i n_p dS \tag{3.7}$$

implies that

$$2V \langle \varepsilon_{ij} \rangle = \int_{S_1} (u_i^{(1)} n_j + u_j^{(1)} n_i) dS + \int_{S_2} (u_i^{(2)} n_j + u_j^{(2)} n_i) dS, \tag{3.8}$$

where S_1 and S_2 are the bounding surfaces of phases 1 and 2, respectively. The surfaces S_1 and S_2 contain the interfaces S_{12} and the external surface S . Assuming perfect bonding between the phases, i.e.

$$u_i^{(1)} = u_i^{(2)} \quad \text{on } S_{12},$$

it follows that the contributions from S_{12} in the two integrals in Eq. (3.8) cancel each other. This leads to

$$\langle \varepsilon_{ij} \rangle = \frac{1}{2V} \int_S (u_i n_j + u_j n_i) dS. \tag{3.9}$$

Substituting in Eq. (3.9) the homogeneous boundary conditions (3.3) and using again the Gauss theorem (3.7) yields

$$\langle \varepsilon_{ij} \rangle = \frac{1}{2V} \int_S (\varepsilon_{ip}^0 x_p n_j + \varepsilon_{jp}^0 x_p n_i) dS = \frac{1}{2V} \varepsilon_{ij}^0 \int_V 2x_{p,i} dV = \varepsilon_{ij}^0, \tag{3.10}$$

where $x_{p,i} = \delta_{pi}$; i.e. the volume averaged strain within RVE is equal to the constant strain applied on the surface.

The homogeneous boundary conditions with traction applied on S , produce a stress field in the composite whose average, $\langle \sigma_{ij} \rangle$, is identical to the constant stress σ_{ij}^0 . To this end, consider the equilibrium equations in the absence of body forces

$$\sigma_{ij,j} = 0, \tag{3.11}$$

which implies that

$$(\sigma_{ik} x_j)_{,k} = \sigma_{ik,k} x_j + \sigma_{ij} x_{j,k} = \sigma_{ij} \delta_{jk} = \sigma_{ij}. \tag{3.12}$$

Substituting this relation in (3.1) provides

$$V \langle \sigma_{ij} \rangle = \int_V (\sigma_{ik} x_j)_{,k} dV$$

and by Gauss' theorem we have

$$V \langle \sigma_{ij} \rangle = \int_{S_1} \sigma_{ik}^{(1)} x_j n_k^{(1)} ds + \int_{S_2} \sigma_{ik}^{(2)} x_j n_k^{(2)} ds \quad (3.13)$$

Since tractions are continuous at the interfaces S_{12} , i.e.

$$\sigma_{ij}^{(1)} n_j^{(1)} = -\sigma_{ij}^{(2)} n_j^{(2)} \quad \text{on } S_{12},$$

the contributions from S_{12} to the two integrals cancel each other and Eq. (3.13) reduces to

$$V \langle \sigma_{ij} \rangle = \int_S \sigma_{ik} x_j n_k ds = \sigma_{ij}^{(0)} \int_S x_j n_k dS = \sigma_{ik}^{(0)} \int_V x_{jk} dV = V \sigma_{ik}^{(0)}.$$

Thus

$$\langle \sigma_{ij} \rangle = \sigma_{ij}^{(0)}. \quad (3.14)$$

3.2.2. Relation between averages. Let us consider the homogeneous boundary conditions (3.3) according to which displacements are applied on the surface S of a RVE. For a two-phase composite with perfect bonding between the constituents

$$\langle \varepsilon_{ij} \rangle = c_1 \langle \varepsilon_{ij} \rangle^{(1)} + c_2 \langle \varepsilon_{ij} \rangle^{(2)}, \quad (3.15)$$

where c_α with $\alpha = 1, 2$ denote the volume fractions of the phases, and

$$\langle \varepsilon_{ij} \rangle^{(\alpha)} = \frac{1}{V_\alpha} \int_{V_\alpha} \varepsilon_{ij}^{(\alpha)} dv \quad (3.16)$$

which is the average strain in the phase α . Similarly,

$$\langle \sigma_{ij} \rangle^{(\alpha)} = \frac{1}{V_\alpha} \int_{V_\alpha} \sigma_{ij}^{(\alpha)} dv \quad (3.17)$$

and

$$\langle \sigma_{ij} \rangle = c_1 \langle \sigma_{ij} \rangle^{(1)} + c_2 \langle \sigma_{ij} \rangle^{(2)}. \quad (3.18)$$

By the average strain theorem we have

$$\langle \varepsilon_{ij} \rangle = \varepsilon_{ij}^{(0)},$$

and the constitutive law in the phases is

$$\langle \sigma_{ij} \rangle^{(\alpha)} = C_{ijkl}^{(\alpha)} \langle \varepsilon_{kl} \rangle^{(\alpha)}, \quad \alpha = 1, 2, \quad (3.19)$$

where $C_{ijkl}^{(\alpha)}$ are stiffnesses of phases.

The constitutive law for a composite can be written in terms of averages

$$\langle \sigma_{ij} \rangle = C_{ijkl}^* \langle \varepsilon_{ij} \rangle, \quad (3.20)$$

where C_{ijkl}^* is as yet unknown stiffness of the composite. From Eqs. (3.10), (3.15), (3.17), (3.18) and (3.19) substituted to Eq. (3.20) one gets

$$\begin{aligned}
 C_{ijkl}^* \langle \varepsilon_{ij} \rangle &= \langle \sigma_{ij} \rangle \\
 C_{ijkl}^* \varepsilon_{kl}^0 &= c_1 \langle \sigma_{ij} \rangle^{(1)} + c_2 \langle \sigma_{ij} \rangle^{(2)} \\
 C_{ijkl}^* \varepsilon_{kl}^0 &= c_1 C_{ijkl}^{(1)} \langle \varepsilon_{kl} \rangle^{(1)} + c_2 C_{ijkl}^{(2)} \langle \varepsilon_{kl} \rangle^{(2)} \\
 C_{ijkl}^* \varepsilon_{kl}^0 &= C_{ijkl}^{(1)} \left(\langle \varepsilon_{kl} \rangle - c_2 \langle \varepsilon_{kl} \rangle^{(2)} \right) + c_2 C_{ijkl}^{(2)} \langle \varepsilon_{kl} \rangle^{(2)} \\
 C_{ijkl}^* \varepsilon_{kl}^0 &= C_{ijkl}^{(1)} \varepsilon_{kl}^0 + c_2 \left(C_{ijkl}^{(2)} - C_{ijkl}^{(1)} \right) \langle \varepsilon_{kl} \rangle^{(2)}.
 \end{aligned} \tag{3.21}$$

Equation (3.21) implies that the effective moduli can be determined from the elastic moduli of the phases provided the average strain $\langle \varepsilon_{kl} \rangle^{(2)}$ in the inclusion phase 2 is known.

3.2.3. The Eshelby solution. The case where a given material is infinitely extended is of particular interest for the mathematical simplicity of the solution as well as for its practical importance. When the solution is applied to inclusion problems, it can be assumed with sufficient accuracy that the materials are infinitely extended since the size of the inclusions is relatively small compared to the size of the macroscopic material samples.

Definitions:

Eigenstrain – nonelastic strains such as thermal expansion, phase transformation, initial strains.

Eigenstress – self-equilibrated internal stress caused by one or several of these eigenstrains in bodies which are free from any other external force and surface constraints.

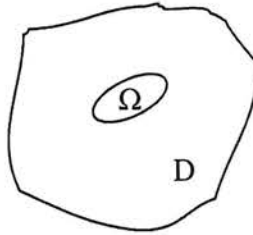
The term “residual stresses” have been frequently used for the self-equilibrated internal stresses when they remain in the material after fabrication or plastic deformation. Eigenstresses are called thermal stresses when thermal expansion is a cause of the corresponding elastic field. For example, when a part Ω of a material has its temperature raised by T , thermal stress σ_{ij} is induced in D by the constraint from the part which surrounds Ω , Fig. 32.

The thermal expansion αT , where α is the linear thermal expansion coefficient, constitutes the thermal expansion strain

$$\varepsilon_{ij}^* = \alpha T \delta_{ij},$$

where δ_{ij} is the Kronecker delta. The thermal expansion strain caused when Ω can be expanded freely with the removal of the constraint from the surrounding part.

The actual strain is then the sum of the thermal stress by Hooke's law. The thermal expansion strain is a typical example of an eigenstrain. In the elastic theory of eigenstrains and eigenstresses, however, it is not necessary to attribute ε_{ij}^* to any specific source. The source could be phase transformation, precipitation, plastic deformation or a fictitious source necessary for the equivalent inclusion method.

FIGURE 32. Inclusion Ω .

When an eigenstrain ε_{ij}^* is prescribed in a finite subdomain Ω in a homogeneous material D , and it is zero in the matrix $D-\Omega$, then Ω is called an *inclusion*. The elastic moduli of the inclusion Ω and the matrix $D-\Omega$ are the *same*.

If a subdomain Ω in a material D has elastic moduli *different* from those of the matrix $D-\Omega$, then Ω is called an *inhomogeneity*. Applied stresses will be disturbed by the existence of the inhomogeneity. This disturbed stress field will be simulated by an eigenstress field by considering a fictitious eigenstrain ε_{ij}^* in Ω in a homogeneous material.

The major contribution made by Eshelby was to establish the relation

$$\varepsilon_{ij}^{(2)\text{total}} = S_{ijkl} \varepsilon_{kl}^* \quad \text{in } \Omega, \quad (3.22)$$

where the total strain in Ω is given by the sum of the eigenstrain and the resulting elastic strain i.e.

$$\varepsilon_{ij}^{(2)\text{total}} = \varepsilon_{ij}^{(2)} + \varepsilon_{ij}^*. \quad (3.23)$$

The eigenstrain ε_{ij}^* is uniform in Ω and the resulting strain (3.23) is also uniform in Ω . This is the most valuable result from the Eshelby solution. (The development of Eq. (3.22) is omitted here). In the expression (3.22) S_{ijkl} is called Eshelby tensor which has the following properties:

- it is symmetric with respect to the first two indices and the second two indices

$$S_{ijkl} = S_{jikl} = S_{ijlk},$$

however, it is not, in general, symmetric with respect to the exchange of ij and kl , i.e.

$$S_{ijkl} \neq S_{klij};$$

- it is independent of the material properties of the inclusion Ω ;
- it is completely defined in terms of the aspect ratios of the ellipsoidal inclusion Ω and the elastic parameters of the surrounding matrix $D-\Omega$;
- when the surrounding matrix $D-\Omega$ is isotropic, then S_{ijkl} depends only on the Poisson ratio of the matrix and the aspect ratios of Ω .

If an ellipsoidal inclusion has its principal half axes denoted by a_1 , a_2 and a_3 then the Eshelby tensor components for special shapes of inclusions are as follows:

Sphere ($a_1 = a_2 = a_3$):

$$S_{1122} = S_{2233} = S_{1133} = S_{1133} = S_{2211} = S_{3322} = \frac{5\nu - 1}{15(1 - \nu)},$$

$$S_{1212} = S_{2323} = S_{3131} = \frac{4 - 5\nu}{15(1 - \nu)},$$

$$S_{1111} = S_{2222} = S_{3333} = \frac{7 - 5\nu}{15(1 - \nu)}.$$

Elliptic cylinder ($a_3 \rightarrow \infty$):

$$S_{1111} = \frac{1}{2(1 - \nu)} \left[\frac{a_2^2 + 2a_1a_2}{(a_1 + a_2)} + (1 - 2\nu) \frac{a_2}{a_1 + a_2} \right],$$

$$S_{2222} = \frac{1}{2(1 - \nu)} \left[\frac{a_1^2 + 2a_1a_2}{a_1 + a_2} + (1 - 2\nu) \frac{a_1}{(a_1 + a_2)} \right],$$

$$S_{3333} = 0,$$

$$S_{1122} = \frac{1}{2(1 - \nu)} \left[\frac{a_2^2}{(a_1 + a_2)} - (1 - 2\nu) \frac{a_2}{a_1 + a_2} \right],$$

$$S_{2233} = \frac{1}{2(1 - \nu)} \frac{2\nu a_1}{a_1 + a_2},$$

$$S_{3311} = 0,$$

$$S_{2233} = \frac{1}{2(1 - \nu)} \left[\frac{2\nu a_1}{a_1 + a_2} \right],$$

$$S_{3311} = 0,$$

$$S_{1133} = \frac{1}{2(1 - \nu)} \frac{2\nu a_2}{a_1 + a_2},$$

$$S_{2211} = \frac{1}{2(1 - \nu)} \left[\frac{a_1^2}{(a_1 + a_2)^2} - (1 - 2\nu) \frac{a_1}{a_1 + a_2} \right],$$

$$S_{3322} = 0,$$

$$S_{1212} = \frac{1}{2(1 - \nu)} \left[\frac{a_1^2 + a_2^2}{2(a_1 + a_2)^2} + \frac{1 - 2\nu}{2} \right],$$

$$S_{2323} = \frac{a_1}{2(a_1 + a_2)},$$

$$S_{3131} = \frac{a_2}{2(a_1 + a_2)}.$$

Penny shape ($a_1 = a_2 \gg a_3$):

$$\begin{aligned}
 S_{1111} &= S_{2222} = \frac{13 - 8\nu}{32(1 - \nu)} \pi \frac{a_3}{a_1}, \\
 S_{3333} &= 1 - \frac{1 - 2\nu}{1 - \nu} \frac{\pi a_3}{4 a_1}, \\
 S_{1122} &= S_{2211} = \frac{8\nu - 1}{32(1 - \nu)} \pi \frac{a_3}{a_1}, \\
 S_{1133} &= S_{2233} = \frac{2\nu - 1}{8(1 - \nu)} \pi \frac{a_3}{a_1}, \\
 S_{3311} &= S_{3322} = \frac{\nu}{1 - \nu} \left(1 - \frac{4\nu + 1}{8\nu} \pi \frac{a_3}{a_1} \right), \\
 S_{1212} &= \frac{7 - 8\nu}{32(1 - \nu)} \pi \frac{a_3}{a_1}, \\
 S_{1313} &= S_{2323} = \frac{1}{2} \left(1 + \frac{\nu - 2}{1 - \nu} \frac{\pi a_3}{4 a_1} \right);
 \end{aligned}$$

when $a_3 \rightarrow \infty$:

$$\begin{aligned}
 S_{2323} &= S_{3131} = \frac{1}{2}, \\
 S_{3311} &= S_{3322} = \frac{\nu}{1 - \nu}, \\
 S_{3333} &= 1,
 \end{aligned}$$

and all other $S_{ijkl} = 0$.

3.2.4. Equivalent inclusion method. Consider an infinitely extended material with the elastic moduli $C_{ijkl}^{(1)}$ containing an ellipsoidal inhomogeneity with the elastic moduli $C_{ijkl}^{(2)}$. We investigate the disturbance in an applied stress caused by the presence of this inhomogeneity. Let us denote the applied stress at infinity by σ_{ij}^0 and the corresponding strain ε_{ij}^0 . The stress disturbance and the strain disturbance are denoted by $\sigma_{ij}^{(\alpha)}$ and $\varepsilon_{ij}^{(\alpha)}$, $\alpha = 1, 2$, respectively. The total stress (actual stress) is $\sigma_{ij}^0 + \sigma_{ij}^{(1)}$ in the matrix and $\sigma_{ij}^0 + \sigma_{ij}^{(2)}$ in the inhomogeneity. The total strains are $\varepsilon_{ij}^0 + \varepsilon_{ij}^{(1)}$ and $\varepsilon_{ij}^0 + \varepsilon_{ij}^{(2)}$, respectively. Hooke's law is written

$$\begin{aligned}
 \sigma_{ij}^0 + \sigma_{ij}^{(2)} &= C_{ijkl}^{(2)} \left(\varepsilon_{kl}^0 + \varepsilon_{kl}^{(2)} \right) \quad \text{in } \Omega, \\
 \sigma_{ij}^0 + \sigma_{ij}^{(1)} &= C_{ijkl}^{(1)} \left(\varepsilon_{kl}^0 + \varepsilon_{kl}^{(1)} \right) \quad \text{in } D - \Omega.
 \end{aligned} \tag{3.24}$$

The equivalent inclusion method is used to simulate the stress disturbance using the eigenstress resulting from an inclusion which occupies the domain Ω . Consider an

infinitely extended homogeneous material with the elastic moduli $C_{ijkl}^{(1)}$ everywhere, containing domain Ω with an eigenstrain ε_{ij}^* , Fig. 33. The eigenstrain has been introduced here arbitrarily in order to simulate the inhomogeneity problem using the inclusion problem.

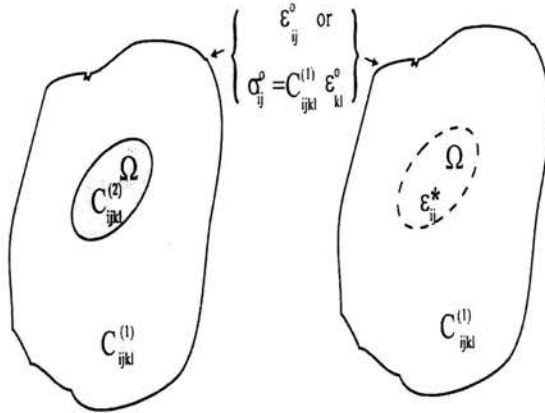


FIGURE 33. Equivalent inclusion method.

When this homogeneous material is subjected to the applied strain ε_{ij}^0 at infinity, the resulting total stress in the inclusion is

$$\sigma_{ij}^0 + \sigma_{ij}^{(2)} = C_{ijkl}^{(1)} \left(\varepsilon_{kl}^0 + \varepsilon_{kl}^{(2)\text{total}} - \varepsilon_{kl}^* \right) \quad \text{in } \Omega. \quad (3.25)$$

The necessary and sufficient condition for the equivalency of the stresses and strains in the above two problems of the inhomogeneity and inclusion is an identity between Eqs. (3.24)₁ and (3.25) i.e.

$$C_{ijkl}^{(2)} \left(\varepsilon_{kl}^0 + \varepsilon_{kl}^{(2)} \right) = C_{ijkl}^{(1)} \left(\varepsilon_{kl}^0 + \varepsilon_{kl}^{(2)\text{total}} - \varepsilon_{kl}^* \right), \quad (3.26)$$

where $\varepsilon_{kl}^{(2)\text{total}} - \varepsilon_{kl}^* = \varepsilon_{kl}^{(2)}$ is the elastic strain in the inclusion, Eq. (3.23). For the inhomogeneity problem (i.e. left hand side of Eq. (3.26)) the strain $\varepsilon_{kl}^{(2)}$ is equal to the total strain $\varepsilon_{kl}^{(2)\text{total}}$, then from Eqs. (3.26) and (3.22) one gets

$$C_{ijk}^{(2)} \left(\varepsilon_{kl}^0 + S_{klmn} \varepsilon_{mn}^* \right) = C_{ijkl}^{(1)} \left(\varepsilon_{kl}^0 + S_{klmn} \varepsilon_{mn}^* - \varepsilon_{kl}^* \right). \quad (3.27)$$

Knowing elastic constants of the inhomogeneity and the matrix together with the Eshelby tensor, it is possible to find from Eq. (3.27) components of the eigenstrain ε_{ij}^* in terms of the remote strain ε_{ij}^0 . After obtaining ε_{ij}^* the stress in the inhomogeneity $\sigma_{ij}^0 + \sigma_{ij}^{(2)}$ may be obtained from Eq. (3.24)₁ or Eq. (3.25).

In a RVE there is a unique dependence of the average strains in the phases upon the overall strain in the composite. Let this be written as

$$\begin{aligned} \langle \varepsilon_{ij} \rangle^{(1)} &= A_{ijkl}^{(1)} \langle \varepsilon_{kl} \rangle = A_{ijkl}^{(1)} \varepsilon_{kl}^0, \\ \langle \varepsilon_{ij} \rangle^{(2)} &= A_{ijkl}^{(2)} \varepsilon_{kl}^0, \end{aligned} \quad (3.28)$$

with

$$c_1 A_{ijkl}^{(1)} + c_2 A_{ijkl}^{(2)} = I_{ijkl},$$

where I_{ijkl} is the unit tensor; $A_{ijkl}^{(\alpha)}$ ($\alpha = 1, 2$) are called concentration tensors. Then, substituting the average strain in the inclusion phase 2, i.e. Eq. (3.28)₂ to the expression (2.21) the required effective stiffness of the composite can be obtained as

$$C_{ijkl}^* = C_{ijkl}^{(1)} + c_2 \left(C_{ijmn}^{(2)} - C_{ijmn}^{(1)} \right) A_{mnkl}^{(2)}. \quad (3.29)$$

From Eq. (3.29) it is clear that the knowledge of the concentration tensor is sufficient to determine the effective stiffness of a composite provided that the constituent properties and volume fractions of phases are known. This being a tremendously difficult task, different models have been introduced which approximate the concentration tensor.

The simplest model follows from the Eshelby concept and is called the “dilute” approximation, in which the concentration tensor is approximated by embedding a single particle in an all-matrix material. In the “dilute” approximation the volume fraction of particles is small enough that each single particle does not “see and feel” its neighbours, and therefore they may be considered independently. Since the distances between particles are large as compared to dimensions of the particles we may consider each particle embedded in the infinite matrix. (In a sequel, the tensor quantities will be denoted with lower dash in order to shorten the notation). Then from Eq. (3.28)₂

$$\mathbf{A}^{(2)} = \frac{\boldsymbol{\varepsilon}^{(2)}}{\boldsymbol{\varepsilon}^0}. \quad (3.30)$$

The strain in the inhomogeneity

$$\boldsymbol{\varepsilon}^{(2)} = \boldsymbol{\varepsilon}^{(2)\text{total}} + \boldsymbol{\varepsilon}^0 \quad (3.31)$$

or

$$\boldsymbol{\varepsilon}^{(2)} = \mathbf{S} \boldsymbol{\varepsilon}^* + \boldsymbol{\varepsilon}^0. \quad (3.32)$$

It follows from Eq. (3.26) and Eq. (3.32) that

$$\mathbf{C}^{(1)} \left(\boldsymbol{\varepsilon}^{(2)} - \boldsymbol{\varepsilon}^* \right) = \mathbf{C}^{(2)} \boldsymbol{\varepsilon}^{(2)}$$

or

$$\mathbf{C}^{(1)} \boldsymbol{\varepsilon}^* = \left(\mathbf{C}^{(1)} - \mathbf{C}^{(2)} \right) \boldsymbol{\varepsilon}^{(2)}. \quad (3.33)$$

From the Eshelby solution (3.22) the eigenstrain can be calculated as

$$\boldsymbol{\varepsilon}^* = \mathbf{S}^{-1} \boldsymbol{\varepsilon}^{(2)\text{total}}$$

or

$$\boldsymbol{\varepsilon}^* = \mathbf{S}^{-1} \left(\boldsymbol{\varepsilon}^{(2)} - \boldsymbol{\varepsilon}^0 \right), \quad (3.34)$$

where \mathbf{S}^{-1} is an inverse Eshelby tensor. Then substituting (3.34) into (3.33) yields

$$\mathbf{C}^{(1)} \left[\mathbf{S}^{-1} \left(\boldsymbol{\varepsilon}^{(2)} - \boldsymbol{\varepsilon}^0 \right) \right] = \left(\mathbf{C}^{(1)} - \mathbf{C}^{(2)} \right) \boldsymbol{\varepsilon}^{(2)}$$

or

$$\left[\mathbf{C}^{(1)}\mathbf{S}^{-1} - \left(\mathbf{C}^{(1)} - \mathbf{C}^{(2)} \right) \right] \boldsymbol{\varepsilon}^{(2)} = \mathbf{C}^{(1)}\mathbf{S}^{-1}\boldsymbol{\varepsilon}^0 \tag{3.35}$$

Multiplication by $\mathbf{S}[\mathbf{C}^{(1)}]^{-1}$ provides

$$\left\{ \mathbf{I} - \mathbf{S} \left[\mathbf{C}^{(1)} \right]^{-1} \left(\mathbf{C}^{(1)} - \mathbf{C}^{(2)} \right) \right\} \boldsymbol{\varepsilon}^{(2)} = \boldsymbol{\varepsilon}^0 \tag{3.36}$$

It follows that the requested concentration tensor of an elliptical inclusion, embedded in a matrix subjected to uniform deformation at large distances from the inclusion, is given by

$$\mathbf{A}^{(2)} = \frac{\boldsymbol{\varepsilon}^{(2)}}{\boldsymbol{\varepsilon}^0} = \left\{ \mathbf{I} - \mathbf{S} \left[\mathbf{C}^{(1)} \right]^{-1} \left(\mathbf{C}^{(1)} - \mathbf{C}^{(2)} \right) \right\}^{-1} \tag{3.37}$$

and the effective stiffness can be determined from Eq. (3.29).

Typical results are shown in Fig. 34, which gives axial and transverse stiffness prediction for aligned short fibre composites where the short fibre was modelled as an elongated ellipsoid with the aspect ratio of $a_3/a_1 = a_2$ varying from 1 to 100. Figure 34a confirms that in the practicable volume fraction range up to about 40-50%, fibres with fairly high aspect ratios are needed in order to effect substantial improvements in the stiffness. The transverse stiffness predictions in Fig. 34b, however, show clearly that the aspect ratio has very little effect on the transverse stiffness. This is the case for all composites.

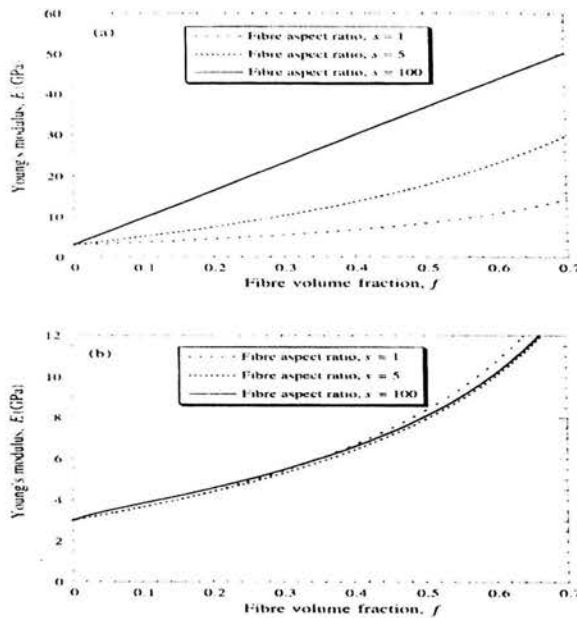


FIGURE 34. Eshelby predictions of the Young's modulus as a function of fibre volume fraction for glass fibres in an epoxy matrix for (a) axial and (b) transverse loading.

3.2.5. The Mori-Tanaka theory. An equivalent inclusion method provides a first-order approximation and yields an explicit result for a composite stiffness \mathbf{C}^* but neglects particle interaction and is therefore valid only at small concentration of particles. A better approximation, which takes into account particle interactions, is the Mori-Tanaka theory. This method assumes that the average strain $\langle \epsilon \rangle^{(2)}$ in the interacting inhomogeneities can be approximated by that of a single inhomogeneity embedded in an infinite matrix subjected to the uniform *average matrix strain* $\langle \epsilon \rangle^{(1)}$. This is illustrated in Fig. 35.

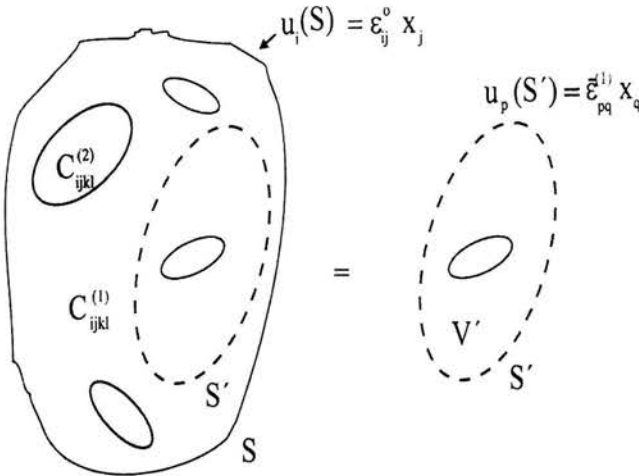


FIGURE 35. Schematic representation of the Mori-Tanaka model.

The problem to be solved according to this model is that of a single inhomogeneity in a certain large volume V' which is enclosed by a surface S' , and subjected to the boundary condition

$$u_p(S') = \langle \epsilon_{pq} \rangle^{(1)} x_q. \quad (3.38)$$

The solution of this problem is

$$\langle \epsilon_{mn} \rangle^{(2)} = T_{mnpq} \langle \epsilon_{pq} \rangle^{(1)}, \quad (3.39)$$

where \mathbf{T} is determined from the solution of a single inhomogeneity embedded in an infinite matrix subjected to boundary conditions (3.38).

Substituting (3.39) into expression (3.15) and remembering the statement of the average strain theorem (Eq. (3.10)) yields (in shortened notation)

$$\epsilon^0 = c_1 \langle \epsilon \rangle^{(1)} + c_2 \mathbf{T} \langle \epsilon \rangle^{(1)}$$

or

$$\langle \epsilon \rangle^{(1)} = (c_1 \mathbf{I} + c_2 \mathbf{T})^{-1} \epsilon^0. \quad (3.40)$$

Substituting Eq. (3.40) into (3.39) leads to the following relation

$$\mathbf{A}^{(2)} = \frac{\langle \boldsymbol{\varepsilon} \rangle^{(2)}}{\boldsymbol{\varepsilon}^0} = \mathbf{T}(c_1 \mathbf{I} + c_2 \mathbf{T})^{-1}. \tag{3.41}$$

Thus, the concentration tensor $\mathbf{A}^{(2)}$, which relates an average strain in the inhomogeneity to the uniform remote strain field, is related to the concentration tensor \mathbf{T} via Eq. (3.41). Consequently, the effective stiffness of the composite is given from Eqs. (3.29) and (3.41) as

$$\mathbf{C}^* = \mathbf{C}^{(1)} + c_2(\mathbf{C}^{(2)} - \mathbf{C}^{(1)})\mathbf{T}(c_1 \mathbf{I} + c_2 \mathbf{T})^{-1}. \tag{3.42}$$

The concentration tensor \mathbf{T} is determined from the solution of a single inhomogeneity embedded in an infinite matrix subjected to boundary conditions (3.38). From the Eshelby equivalent inclusion method, Eq. (3.27), we have

$$\mathbf{C}^{(2)} \left(\langle \boldsymbol{\varepsilon} \rangle^{(1)} + \mathbf{S} \boldsymbol{\varepsilon}^* \right) = \mathbf{C}^{(1)} \left(\langle \boldsymbol{\varepsilon} \rangle^{(1)} + \mathbf{S} \boldsymbol{\varepsilon}^* - \boldsymbol{\varepsilon}^* \right), \tag{3.43}$$

where $\boldsymbol{\varepsilon}^0$ has been replaced by the average matrix strain $\langle \boldsymbol{\varepsilon} \rangle^{(1)}$ since now it constitutes the homogeneous boundary conditions. For the inhomogeneity the strain is given by

$$\langle \boldsymbol{\varepsilon} \rangle^{(2)} = \boldsymbol{\varepsilon}^{(2)\text{total}} + \langle \boldsymbol{\varepsilon} \rangle^{(1)} = \mathbf{S} \boldsymbol{\varepsilon}^* + \langle \boldsymbol{\varepsilon} \rangle^{(1)}. \tag{3.44}$$

The expression (3.44) is analogous to (3.32) with an appropriate replacement of the remote strain field. Then, calculating the eigenstrain from (3.44), i.e.

$$\boldsymbol{\varepsilon}^* = \mathbf{S}^{-1} \left(\langle \boldsymbol{\varepsilon} \rangle^{(2)} - \langle \boldsymbol{\varepsilon} \rangle^{(1)} \right),$$

and substituting to Eq. (3.43) with (3.44) in mind yields

$$\begin{aligned} \mathbf{C}^{(2)} \langle \boldsymbol{\varepsilon} \rangle^{(2)} &= \mathbf{C}^{(1)} \left(\langle \boldsymbol{\varepsilon} \rangle^{(2)} - \boldsymbol{\varepsilon}^* \right) \\ &\Downarrow \\ \mathbf{C}^{(1)} \boldsymbol{\varepsilon}^* &= \left(\mathbf{C}^{(1)} - \mathbf{C}^{(2)} \right) \langle \boldsymbol{\varepsilon} \rangle^{(2)} \\ &\Downarrow \\ \mathbf{C}^{(1)} \mathbf{S}^{-1} \left(\langle \boldsymbol{\varepsilon} \rangle^{(2)} - \langle \boldsymbol{\varepsilon} \rangle^{(1)} \right) &= \left(\mathbf{C}^{(1)} - \mathbf{C}^{(2)} \right) \langle \boldsymbol{\varepsilon} \rangle^{(2)} \\ &\Downarrow \\ \left[\mathbf{C}^{(1)} \mathbf{S}^{-1} - \left(\mathbf{C}^{(1)} - \mathbf{C}^{(2)} \right) \right] \langle \boldsymbol{\varepsilon} \rangle^{(2)} &= \mathbf{C}^{(1)} \mathbf{S}^{-1} \langle \boldsymbol{\varepsilon} \rangle^{(1)}. \end{aligned} \tag{3.45}$$

Multiplication of both sides of the Eq. (3.45) by a factor $\mathbf{S}^{-1}(\mathbf{C}^{(1)})^{-1}$ yields

$$\left[\mathbf{I} - \mathbf{S} \left(\mathbf{C}^{(1)} \right)^{-1} \left(\mathbf{C}^{(1)} - \mathbf{C}^{(2)} \right) \right] \langle \boldsymbol{\varepsilon} \rangle^{(2)} = \langle \boldsymbol{\varepsilon} \rangle^{(1)},$$

and recalling the definition of the concentration tensor \mathbf{T} , Eq. (3.39) one obtains

$$\mathbf{T} = \left[\mathbf{I} - \mathbf{S} \left(\mathbf{C}^{(1)} \right)^{-1} \left(\mathbf{C}^{(1)} - \mathbf{C}^{(2)} \right) \right]^{-1}. \tag{3.46}$$

Then, finally, the effective stiffness is determined from Eq. (3.42) with the substitution of the expression (3.46).

The engineering constants of the composite can be derived from the stiffness tensor \mathbf{C}^* (Eq. (3.42)) which is too elaborate for manual manipulations and must be evaluated with a computer programme. As an example, the components of the stiffness tensor \mathbf{C}^* have been calculated for a short fibre composite with perfectly aligned fibres modelled as an elliptic cylinder with equal semi-axis $a_1 = a_2$. The numerical values of the stiffness components are as follows

$$[C_{ijkl}] = \begin{bmatrix} 7.450 & 3.428 & 3.179 & 0 & 0 & 0 \\ & 7.450 & 3.179 & 0 & 0 & 0 \\ & & 0.295 & 0 & 0 & 0 \\ & & & 3.082 & 0 & 0 \\ \text{symmetric} & & & & 3.082 & 0 \\ & & & & & 1.590 \end{bmatrix} \cdot 10^{-10} \text{ [GPa]}.$$

The stiffness has been calculated for a nylon PA6/glass fibre composite with 35% volume fraction of fibres. The matrix and the fibre stiffness were, respectively, 3.0 GPa and 73.5 GPa, whereas the Poisson ratio of the matrix was $\nu = 0.33$. From the stiffness components one can extract engineering constants of the composite, and the Young's modulus of the composite along the direction of fibres' alignment reads $E = 27.68$ GPa, whereas the transverse modulus i.e. along the cross section perpendicular to the fibres privilege direction is $E_t = 5.77$ GPa.

It has to be noted that in a real short fibre composite, processed for example by an injection moulding technique, the fibres are neither aligned nor dispersed at random directions. Fibre orientation is controlled by the nature of the flow field during filling of the mould. In general, fibres tend to become aligned parallel to the direction in which the material is becoming elongated (provided the flow is not too turbulent). This is illustrated by the schematic diagram of the flow pattern during injection into a simple rectangular mould, and the corresponding dispersion pattern of fibres, shown in Fig. 36.

In this case, the fibres are well aligned in the outer layers of the moulding, but more randomly oriented towards the core. By predicting the flow behaviour under different injection conditions for specific components, a degree of control over the final fibre orientation pattern is often possible. Figure 37 shows a unit sphere within which one can illustrate the orientation distribution of fibres. If we translate orientation directions of all fibres contained in a RVE towards the unit sphere in such a way that they become attached to the centre point of the sphere, then the direction lines would cross a part of the surface of the unit sphere enclosed by a circle the longitude of which is determined by the angle θ provided that all fibre directions lie in the interval $[0, \theta]$.

The orientation distribution function $g(\theta, \Phi)$ describes a number of fibres directions which cross a unit surface area of the sphere. Assuming that fibre orientations are uniformly distributed with respect to Φ , which is usually the case for injection moulded components, the orientation distribution function depends only upon the

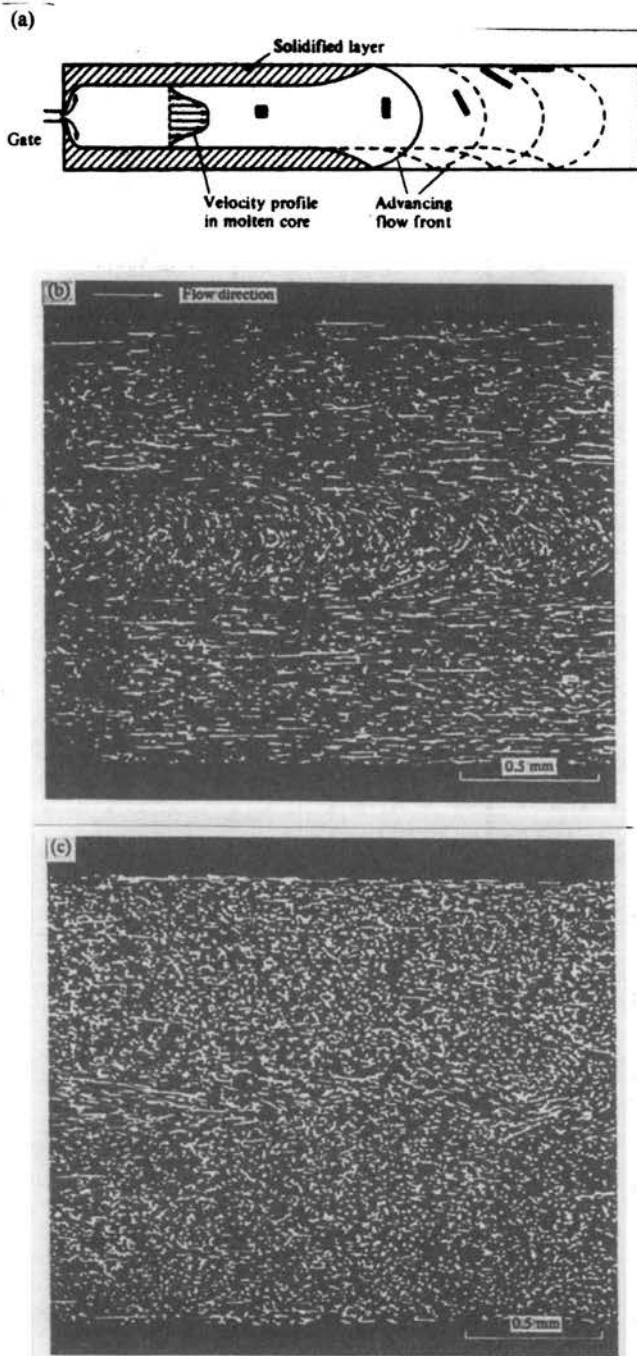


FIGURE 36. (a) Schematic diagram of the mould filling process. (b) The longitudinal section of a polypropylene/15% glass fibre composite. (c) Transverse section from the same moulding.

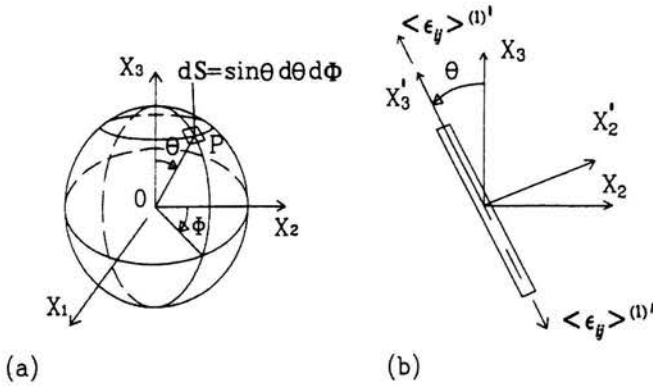


FIGURE 37. (a) Unit sphere. (b) Boundary conditions for a single fibre in local coordinate system.

angle θ , where θ belongs to the interval $[0, \pi/2]$. The boundary conditions for each fibre are described in the local coordinate system (X'_1, X'_2, X'_3) . The local coordinate boundary conditions are obtained from global coordinate boundary conditions which are prescribed for the RVE of the composite, Fig. 38.

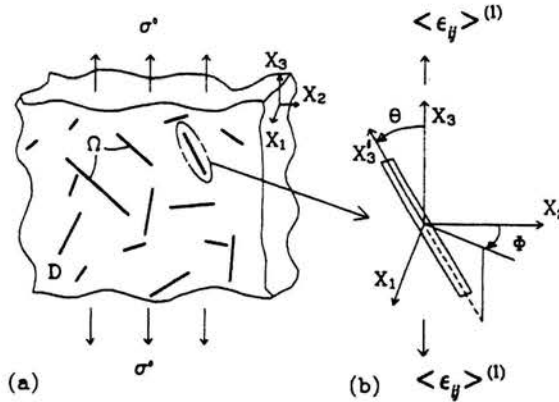


FIGURE 38. (A) RVE. (b) Global coordinate boundary conditions.

The effective stiffness is calculated from an energy balance of the composite

$$\frac{1}{2} \sigma^0 [C^*]^{-1} \sigma^0 = \frac{1}{2} \sigma^0 \epsilon^0 + \frac{1}{2V_D} \int_{\Omega} \sigma^0 \epsilon^* dV,$$

i.e.

$$\sigma^0 = C^{(1)} \epsilon^0 = C^* \left(\epsilon^0 + \frac{1}{V_D} \int_{\Omega} \epsilon^* dV \right)$$

or

$$C^* = \frac{C^{(1)}}{1 + \frac{C^{(1)}}{\sigma^0 V_D} \int_{\Omega} \epsilon^* dV} \tag{3.47}$$

Observe, that in order to find the effective stiffness of the composite it is necessary to estimate eigenstrains ϵ^* . Since each fibre is oriented differently, then the effect of fibres' misalignment (or orientation distribution) is taken into account by averaging the eigenstrain over all directions present in the specimen and characterized by the orientation distribution function i.e.

$$\frac{1}{V_D} \int_{\Omega} \epsilon^* dV = \frac{1}{V_D} \int_0^{\theta} \int_0^{2\pi} \epsilon^*(\theta, \Phi) g(\theta, \Phi) V dS, \tag{3.48}$$

where an infinitesimal surface element is given by

$$dS = \sin \theta d\theta d\Phi.$$

The eigenstrain $\epsilon^*(\theta, \Phi)$ is calculated first in the local coordinate system (X'_1, X'_2, X'_3) following a usual Mori-Tanaka procedure as described above and then transformed into the global coordinate system (X_1, X_2, X_3) becoming a function of angles θ and Φ . The calculations are straightforward but very tedious, and, therefore, omitted here. The volume fraction of fibres c_2 are defined by the following function

$$c_2 = \frac{1}{V_D} \int_{\Omega} g(\theta, \Phi) V dS$$

or

$$\frac{V}{V_D} = \frac{c_2}{\int_{\Omega} g(\theta, \Phi) dS}. \tag{3.49}$$

Substituting (3.49) into (3.48) yields

$$\frac{1}{V_D} \int_{\Omega} \epsilon^* dV = c_2 \frac{\int_0^{\theta} \int_0^{2\pi} \epsilon^*(\theta, \Phi) g(\theta, \Phi) \sin \theta d\theta d\Phi}{\int_0^{\theta} \int_0^{2\pi} g(\theta, \Phi) \sin \theta d\theta d\Phi}. \tag{3.50}$$

One of the most versatile orientation distribution functions is given below

$$g(\theta) = \frac{(\sin \theta)^{2P-1} (\cos \theta)^{2Q-1}}{\int_{\theta_a}^{\theta_b} (\sin \theta)^{2P-1} (\cos \theta)^{2Q-1} d\theta}, \tag{3.51}$$

when the orientation distribution with respect to Φ may be assumed to be uniform. The function (3.51) can simulate a skewness and peakedness of the orientation distribution to different extent depending on numerical values of parameters P and Q ($P, Q > 1/2$). θ_a and θ_b are the upper and lower limit for the angle θ

which is present in the distribution. Figure 39 illustrates an applicability of the expression (3.51) to the description of experimental results. The fibre orientations have been measured by an image analysis system on the cross sections perpendicular to the moulding direction.

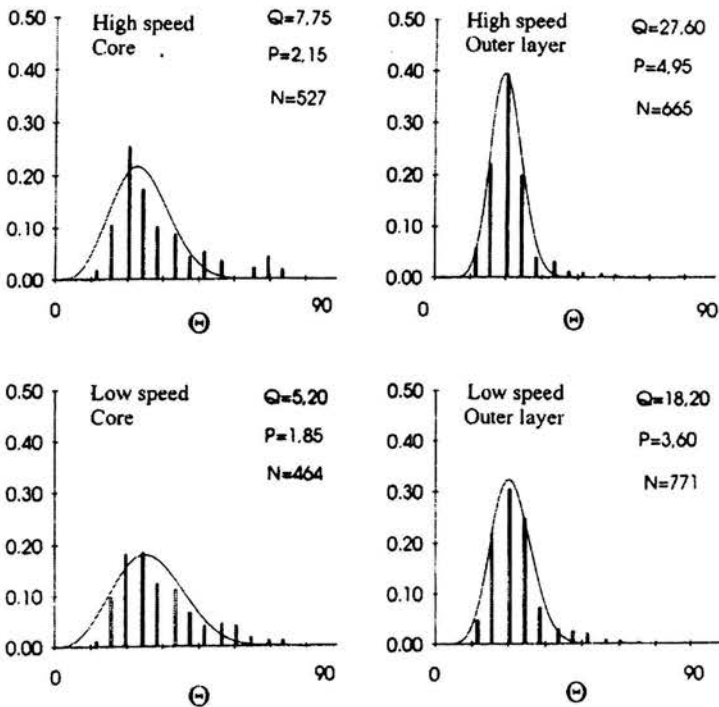


FIGURE 39. Correlation of experimental results (histograms) with the Eq. (3.51). N is a number of measured fibres.

The measurements have been made for two specimens processed with high and low injection speeds, respectively. Moreover, the orientation of fibres has been detected at two positions of each specimen: close to the outer layer of the specimen and at the central area of the core region. Obviously, the fibres are more aligned along the outer layer than in the core of the specimens. It also seems to be the case that the higher injection speed aligns more fibres in the outer layers than the lower speed does.

Since the angle θ prescribes a rotation of the fibre in (X_2, X_3) plane, then the eigenstrain along the X_3 direction is only the function of θ , i.e. $g(\theta, \Phi) = g(\theta, 0)$, under the uniformity assumption with respect to the angle Φ . The Young's modulus along the fibres privileged direction may be calculated from (3.50) yielding

$$E = \frac{E^{(1)}}{1 + \frac{E^{(1)}}{\sigma_3^{(1)}} C_2 \frac{\int_0^{\frac{\pi}{2}} \varepsilon_3^*(\theta,0) g(\theta,0) \sin \theta d\theta}{\int_0^{\frac{\pi}{2}} g(\theta) \sin \theta d\theta}} \tag{3.52}$$

The results were calculated with the same material constants as for a composite with aligned fibres and the experimentally obtained $g(\theta)$, Table 1.

TABLE 1.

	E [Gpa]	
	Outer layer	Core
High speed	9.83	7.28
Low speed	9.13	6.26

It follows that the fibre orientation distribution has a pronounced influence on the composite stiffness. Furthermore, the outer layer of the injection moulded parts is more stressed under a uniform deformation field than the core area. This is due to a higher stiffness resulting from the better alignment of fibres in the region. Thus, the variations of the fibre distribution at different sites of a specimen can by themselves induce nonhomogeneous stress field apart from the disturbances caused by the presence of fibres.

3.2.6. Determination of local stress variations. The determination of the local stress field in a composite is of interest when considering the influence of the microstructure morphology on different micromechanisms such as microcracks and

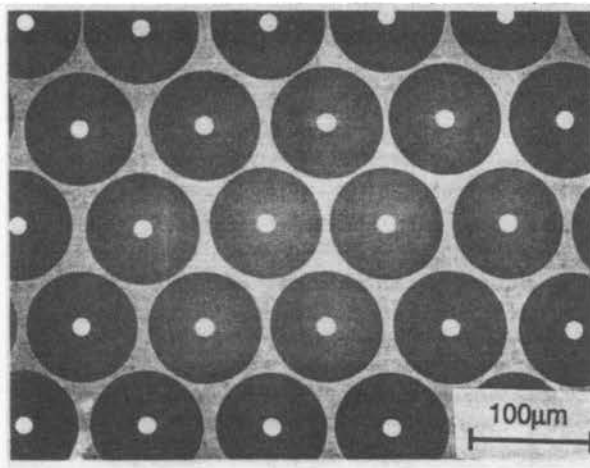


FIGURE 40. Ti-5Al-5V/80% SiC composite.

voids formation and interfacial debonding. Stress analysis methods, which can be applied, are limited by the composition and complexity of the composite, e.g. spatial distribution and shape of the inclusions. For composites with long cylindrical fibres embedded in a matrix material and aligned unidirectionally, the analysis may be performed on a plane section perpendicular to the fibre direction. Thus the analysis may be reduced to a two-dimensional problem consisting of a matrix with circular inclusions.

The spatial distribution of fibres is normally assumed to have some form of regularity. Due to the regularity assumption the fibres will be exposed to the same amount of interaction, and a unit cell (RVE) may consist only of one repeated unit of the regular pattern, such as in Fig. 40.

The example shown in this figure is an exception rather than a common situation. In most composite materials clustering of fibres result in an appearance of matrix-rich areas that significantly influence global response of the material. The

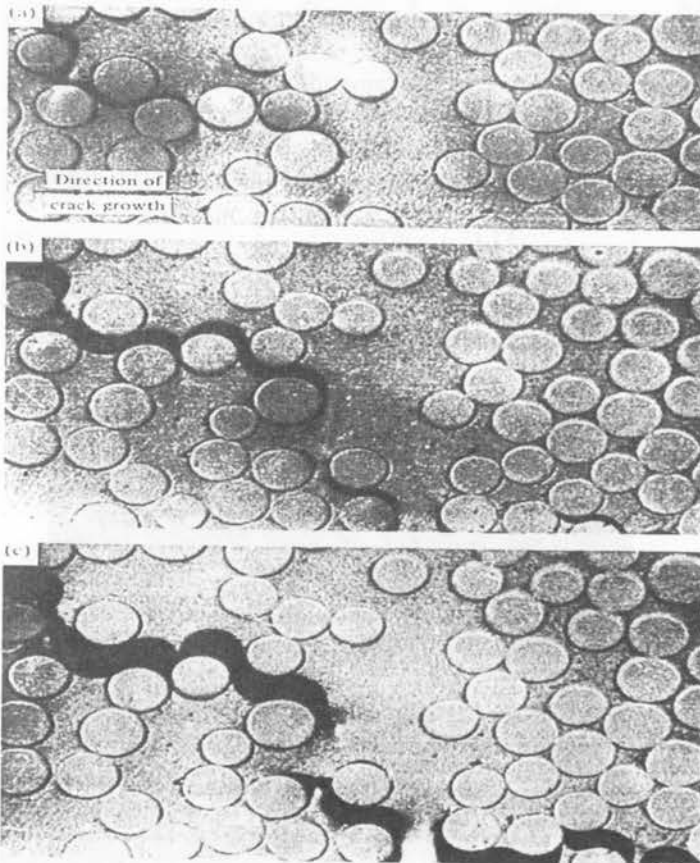


FIGURE 41. Propagation of a transverse crack in polyester/glass lamina.

short range interactions in random distribution of fibres play a dominant role in nonhomogeneous, local variations of the field quantities. These interaction effects produced by fibres are highly sensitive to their exact positions with respect to their neighbours. The local properties become stress-dependent, and the deformation is no longer homogeneous, being influenced by the distribution of the reinforcement phase. Neglecting the geometrical disorder of fibres does not introduce a significant error in the prediction of the elastic and transport properties. By contrast, the fracture and plastic deformation of a matrix are highly nonlinear and localized phenomena which enhance the effect of preexisting heterogeneities in such a way that the local geometrical disorder cannot be neglected. The microfailure threshold is dominated by extreme fluctuations of the stress field, and these local hot spots are strongly influenced by a distribution pattern of fibres. Figure 41 shows the micrograph which illustrates the propagation of a transverse crack in polyester/glass lamina. Obviously, the crack path, i.e. also toughness, depends on how fibres are positioned with respect to each other.

The finite element method is ideally suited to the modelling of highly ordered composite systems, such as a hexagonal array of continuous fibres, because the choice of the mesh domain and its repeat arrangement are unambiguous. The best choice of the mesh for disordered systems is less clear. Unfortunately, in many cases it turns out that the predictions are very sensitive to the arrangement chosen, because it affects the severity of the constraint imposed on different regions of the matrix due to the presence of neighbouring fibres, which, in turn, influences matrix plasticity and damage formation. The finite element solution for a multi-fibre approach is feasible if the mesh resolution is not a critical issue. An example of this is given

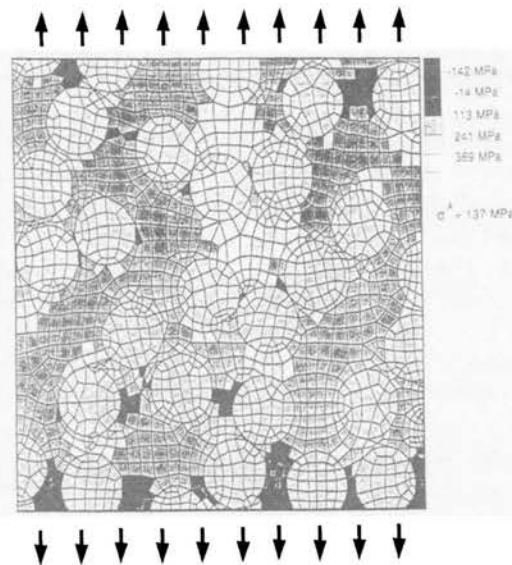


FIGURE 42. Finite element model of randomly packed continuous fibres in a matrix subjected to transverse tensile stress.

in Fig. 42, which illustrates the local variation in matrix hydrostatic stress in a FEM domain containing 30 aligned boron fibres in an Al(6061) matrix subjected to a transverse tensile stress 137 MPa. (The shading of the fibres is not indicative of the stresses within them).

Predicted stress-strain response for this composite is presented in Fig. 43a along with a prediction for different regular distributions. There exists a strong divergence in the plastic response among considered models, and the only cause of these differences is the distribution pattern of fibres. Similarly, in Fig. 43b, large differences in the work-hardening behaviour of short fibre composite result from changes of packing distributions, even though there is no change in fibre volume fraction or aspect ratio, or in any physical property of either constituent (the dashed line in Fig. 43b represents experimental values).

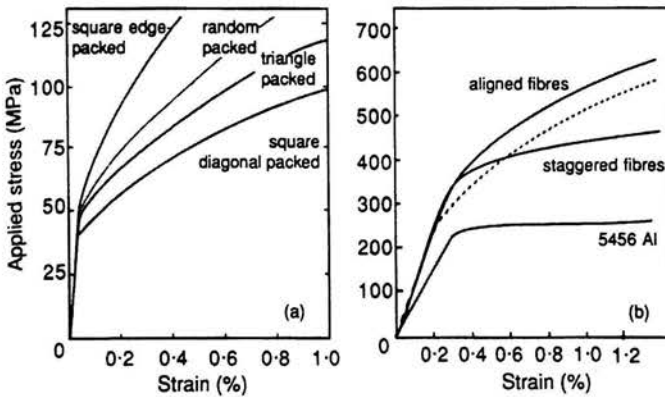


FIGURE 43. Predicted stress-strain responses for (a) Al-50 vol% B long fibre composite under transverse loading, and (b) 5456 Al-20 vol% aspect ratio 4 SiC for different fibre packing.

FE methods are versatile and powerful and can be used to reveal useful information about both local and global characteristics of composites. However, a sound understanding of the basis of FEM such as mesh sensitivity and an appreciation of the significance of the boundary conditions being used are essential, if misleading deductions are to be avoided. Furthermore, in order to explore the influence of fibre dispersions on both local and global quantities, it is necessary to perform a large number of simulations to calculate ensemble-averages within each family of possible dispersions. Finite element application to this task will be too time consuming and costly.

An alternative approach may be based on the combination of the Eshelby's equivalent inclusion method and the superposition scheme which is solved iteratively. Figure 44 illustrates a principal idea behind this method.

Contrary to the solution for a single fibre the stress interactions between the fibres must be taken into account. The basic idea of accounting for this interaction is to determine the stress field inside a fibre as in the Eshelby solution, but also include the interacting stress field from the neighbouring fibres. The problem is

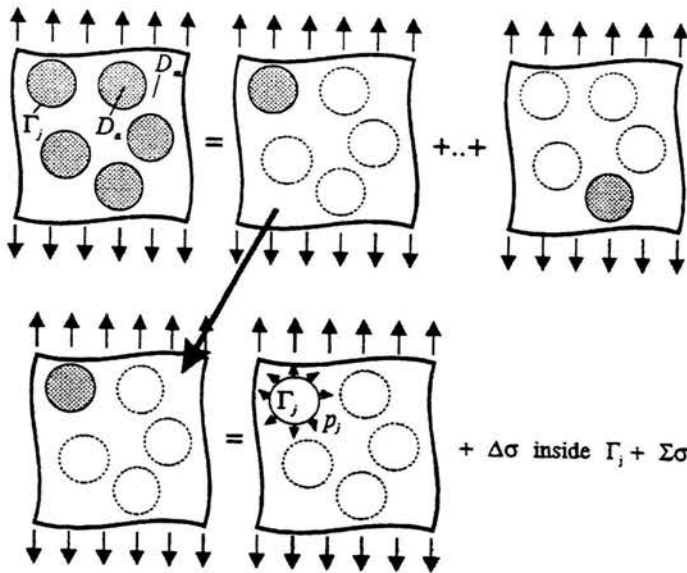


FIGURE 44. Superposition scheme for multi-fibre problem.

divided into a number of sub-problems corresponding to the number of fibres. In each subproblem the heterogeneous solid is substituted with a homogeneous body where an unbalanced stress field has been introduced. This corresponds precisely to the Eshelby idea. However, instead of solving a subproblem directly through the Eshelby tensor, it is solved iteratively since we have to incorporate the interacting stresses from the remaining fibres adding them to the stress field inside the area covered by the fibre. In other words, using Eshelby's terminology, every inclusion in the equivalent material is exposed to the total stress which is composed of the elastic stress and the eigenstress, as before, and additionally has a third component that comes at the inclusion spot from surrounding inhomogeneities. It is obvious that the iterative procedure is necessary as the balance of stresses must be simultaneously achieved at all fibres.

The newest developed X-ray tomographic microscopy method, which is based on the use of desktop instruments, is very suited to yield information about the internal structure of a mm-size composite sample non-destructively and in three dimensions.

X-ray microscopy is a relatively new technique that has not been applied to any significant extent in materials science. Most X-ray microscope development has so far been made using large synchrotron sources. This has limited X-ray microscopy to a research tool available only at the major synchrotron facilities. The use of X-ray tubes with a very small focus together with a very sensitive recording devices enable the design of a bench-top X-ray microscopy with a spatial resolution less than 6 micrometers. In X-ray microtomography, the object is rotated so as to obtain radiographic projections from different viewing angles. An enlarged radiograph

of the object is recorded by an X-ray sensitive camera after the object has been traversed by the conical X-ray beam. All these projections are used in a reconstruction algorithm, which calculates a set of serial non-destructive sections where the interpretation of the image, i.e. cross section, can be done in terms of attenuation of the X-rays in the object. Then, a three-dimensional image of the specimen can be reconstructed from serial sections and can be processed to show and measure three-dimensional features.

Figure 45 shows radiographic image of unidirectional fiber glass epoxy composite acquired at single viewing angle. One reconstructed cross-section through the unidirectional composite is presented in Fig. 46a. This non-destructive image allows determination of the center positions for all fibers in order to characterize a disper-

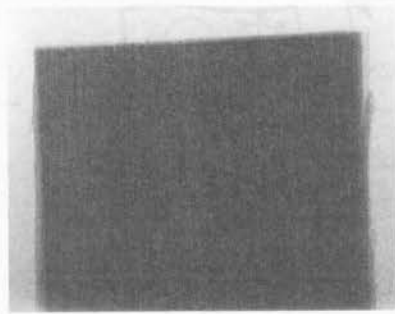


FIGURE 45. Radiographic image of a unidirectional glass fiber epoxy composite.

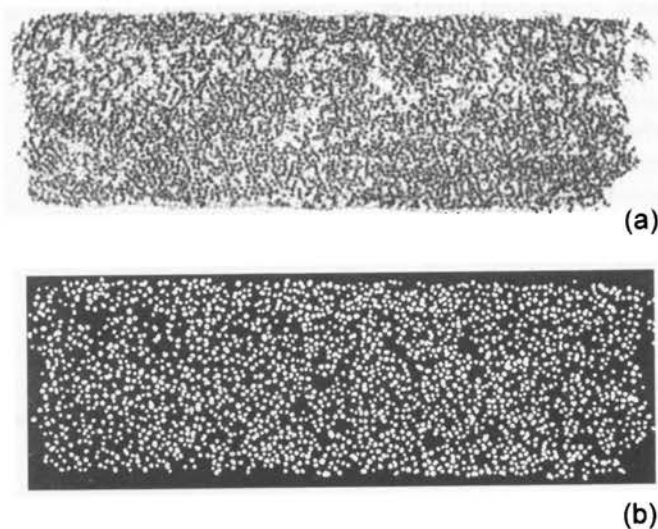


FIGURE 46. reconstructed transverse section of unidirectional composite (a); corresponding binary image (b).

sion pattern in quantitative terms, simultaneously giving a visual impression about the homogeneity of fibers' dispersion.

The precision and accuracy of the image is slightly disturbed by a statistical noise, which cannot be eliminated from microtomographic scans. However, the post-reconstruction filtering, image enhancement and thresholding can to a large extent eliminate its influence. This is illustrated in Fig. 46b where the original image is replaced by its digitized counterpart. The coordinates of fiber centers vary with the position of the reconstructed cross section. The non-destructive slices taken at relatively small interval of approximately $80\ \mu\text{m}$ clearly indicate that the fibers are not parallel. This effect is detailed in Fig. 47, where marked fibers change their relative position along the distance between two consecutive slices. Such non-destructive serial sectioning may be used to disclose fiber waviness, a geometrical factor that controls compressive properties of the unidirectional composite. Having to ones disposal a stress analysis method that allows to calculate the stress field in the uni-

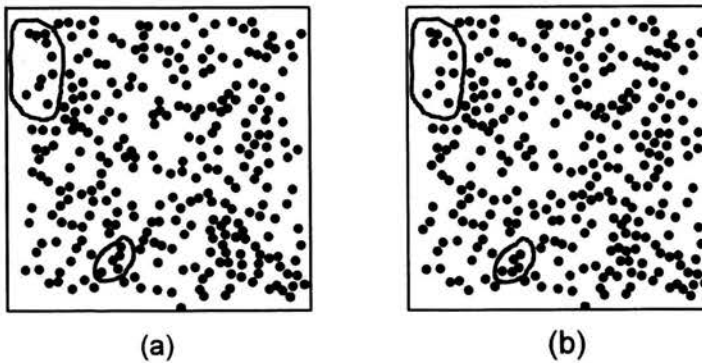


FIGURE 47. Magnified binary reference section (a); section $80\ \mu\text{m}$ apart (b).

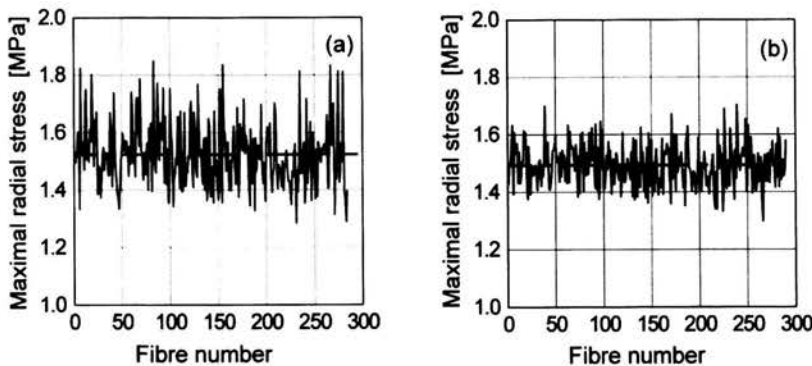


FIGURE 48. Variability of maximal radial stresses for fibers in the reference section (a); in the section $80\ \mu\text{m}$ apart (b).

directional composite loaded transversely to the fibers direction by a remote stress as described above, it is possible to follow slice-to-slice variations of the stress field. Figure 48 exemplifies this possibility showing variability of maximal, radial stresses at fibers' interfaces for two consecutive cross-sections from Fig. 47. The remote stress is equal to 1 MPa; thus all maximal radial stresses are magnified locally. Furthermore, the variability of stresses for the image from Fig. 47a is significantly larger than for the other image. Stress variances are 0.0133 and 0.0057, correspondingly. Although the reconstructed images look apparently very alike a detailed analysis discloses subtle differences that may have a crucial influence on the overall behavior of the composite.

References

Material presented in these lecture notes is based on the following major references:

1. T.W. CHOU, *Microstructural Design of Fiber Composites*, Cambridge University Press, Cambridge 1992.
2. D. HULL and T.W. CLYNE, *An Introduction to Composite Materials*, Cambridge University Press, Cambridge 1996.
3. T.W. CLYNE and P.J. WITHERS, *An Introduction to Metal Matrix Composites*, Cambridge University Press, Cambridge 1995.
4. A. KELLY and C. ZWEBEN [editors-in-chief], *Comprehensive Composite Materials*, Vol.1-6, Elsevier, Amsterdam 2000.

